CHAPTER TWO

Continuous Physical Properties of Cored Marine Sediments

Guillaume St-Onge*, Thierry Mulder, Pierre Francus *and* Bernard Long

Contents

1. Introduction

Continuous centimeter-scale measurements of various physical properties of marine cores now form the basis of most paleoceanographic studies. These

* Corresponding author.

Developments in Marine Geology, Volume 1
ISSN 1572-5480, DOI 10.1016/S1572-5480(07)01007-X

measurements generally provide a rapid and nondestructive method for characterizing the nature and composition of long sedimentary sequences. For major paleoceanographic campaigns such as those carried out as part of the Integrated Ocean Drilling Program (IODP) or the International Marine Past Global Change Study (IMAGES), where sediment samples are used by numerous researchers for various destructive analyses, continuous and nondestructive measurements of physical properties are made quickly onboard and reflect the pristine state of the sediments. Continuous physical properties records provide the basis for stratigraphy and core correlation, the first insight into core lithology, continuous data for time series analyses and a decision tool for determining the best subsampling strategy. Physical properties that are now routinely measured continuously, both onboard and onshore, include: natural gamma radiation, gamma density, *p*-wave velocity, magnetic susceptibility, electrical resistivity and color reflectance. Most of these properties can now be measured continuously and automatically, on whole or split cores placed horizontally or, when the sediment-water interface must remain undisturbed, vertically. Emerging line scan systems and medical techniques may now also be used to continuously image the sediment surface on split cores or the internal structure of whole cores by high-resolution imaging, digital X-ray imaging and computerized coaxial tomography (CAT-scan). The resulting images can then be processed to obtain qualitative and quantitative information about the lithology and/or sedimentary structures of the cores. In this chapter, we first review continuous, cm-scale, nondestructive methods generally used to determine the physical properties of sediments. This is by no means an exhaustive review of all available techniques to measure physical properties of sediment cores, but rather a brief overview of the techniques most commonly used in paleoceanography. The reader is referred to the technical note by Blum (1997) for very detailed information on the measurement protocols for most of the techniques discussed in the first section of this chapter. The second part of this chapter describes emerging methods used both to image and/or determine in 2D or 3D the physical properties of long sedimentary sequences at the millimeter to micrometer-scale, allowing the reconstruction of paleoceanographic or paleoclimatological processes at temporal resolutions on the millennial- to seasonal-scale. The last part of this chapter illustrates some of these new methods using new or recently published data.

2. Continuous Centimeter-Scale Measurements of Physical Properties

The most widely used instrument to measure continuously the physical properties of long marine cores is the Multisensor Track (MST) or Multisensor Core Logger (MSCL; Figure 1). These core loggers were all designed to measure continuously and simultaneously, at the cm-scale, several physical properties such as magnetic susceptibility, gamma density, natural gamma radiation, *p*-wave velocity and electrical resistivity. Although it is generally used as a hand-held technique, we will also briefly discuss the color reflectance measurement method because, as with MSCL sensors, it is fast, nondestructive, high resolution and widely used.

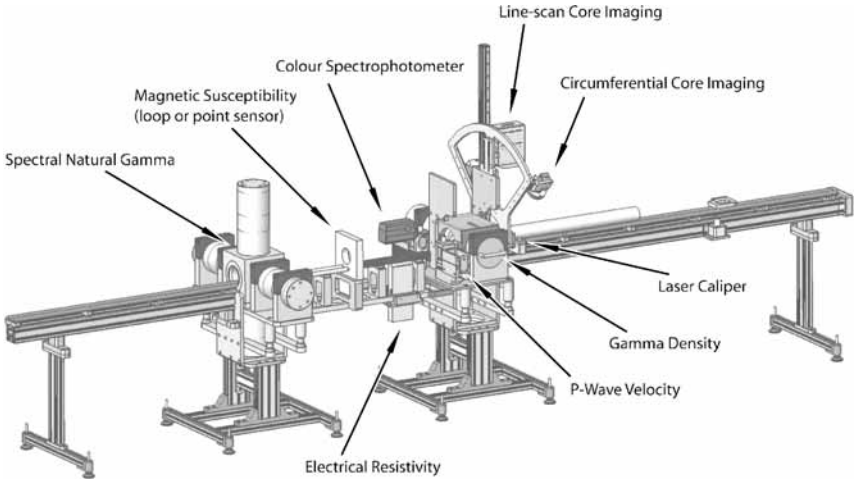

Figure 1 Schematic diagram of a GEOTEK Multisensor Core Logger, MSCL (suitable for both whole or split lined sediment cores and unlined rock cores), illustrating the range of sensor systems available (see text for details). The specific suite of sensors on any given MSCL depends on user requirements and may include a digital X-ray imaging system (not shown).

2.1. Magnetic Susceptibility

Magnetic susceptibility is one of several magnetic properties that can be measured on marine sediment cores. Other magnetic properties are the subject of various books and articles and will not be discussed in this chapter. Stoner and St-Onge (this volume) review the use of magnetic stratigraphy in paleoceanography. Most MSTs or MSCLs can measure the magnetic susceptibility of sediments (Figure 1). Data are generally expressed as uncorrected low field volumetric magnetic susceptibility (k), but may also be expressed either as corrected low field volumetric magnetic susceptibility, if the loop and core diameters are taken into account, or as mass specific magnetic susceptibility, if sediment density is simultaneously measured and taken into account. k provides a first order estimate of ferrimagnetic mineral (e.g., magnetite) abundance in sediments, but is also sensitive to grain size variations, increasing slightly with increasing grain size (e.g., Stoner, Channell, & Hillaire-Marcel, 1996). Although k is generally used to correlate cores on the basis of lithology or to identify rapidly deposited layers (RDL) such as Heinrich events, its potential applications are broader (Thompson & Oldfield, 1986; Maher & Thompson, 1999; Evans & Heller, 2003). One disadvantage of using a magnetic susceptibility loop on whole cores is the rather large response function, resulting in several centimeters of smoothing depending on the loop and core diameters. For instance, Blum (1997) estimated that axial lengths along the core corresponding to more than 99% and 50% (half-height) of the response are approximately 15 and 4.4 cm, respectively, for an 80-mm internal diameter loop. This response function would be even greater for loops of larger diameter. One way to increase the resolution is to use a point-source sensor on split cores. Such an instrument can now be used on an MSCL or a separate track (e.g., the system developed by I. Snowball at Lund University, Figure 2). According to the manufacturer, the sensitive

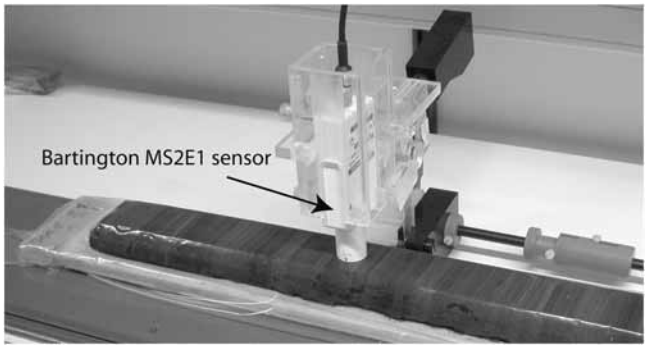

Figure 2 TAMISCAN-TS1 point-source magnetic susceptibility track. The system uses a Bartington MS2E1 sensor. A split core covered by a plastic sheet is being measured.

area of the point sensor probe (50% maximum response) is a 3.8 mm × 10.5 mm rectangle. Another alternative for increasing the resolution is to take continuous measurements on u-channel samples (2 × 2 cm, 1.5 m long plastic liner inserted in the middle of a split section for paleomagnetic measurements) using a smaller diameter loop coupled with a cryogenic magnetometer (e.g., the Gif-sur-Yvette system) or a separate track using a kappa bridge (Thomas, Guyodo, & Channell, 2003). In both cases, the response function (half-height) will be close to 3 cm.

2.2. Gamma Density

In most MSTs or MSCLs, a ^{137}Cs radioactive source and a NaI (TI) detector are used to measure sediment density based on emitted gamma ray attenuation (Figure 1). In general, a beam a few millimeters in diameter is emitted through the source collimators (2.5 or 5 mm), allowing a downcore spatial resolution at the cm-scale. To obtain precise data, the instrument must be properly calibrated using a standard of known density in distilled water. Different standards must be used for split and whole core loggers. In addition, when logging on either split or whole core systems, biases may be introduced by variations in sediment thickness or by the liner thickness itself. The GEOTEK MSCL can now measure sediment thickness variations on split cores. The gamma ray source and detector can also be placed horizontally instead of vertically to reduce possible sediment voids inside the liner due to gravity in whole cores. Clearly, the same liner used for calibration should be used during coring. Because density yields information on sediment properties such as grain size and mineralogy, the measurement of gamma density is a very widely used method.

2.3. *P*-Wave Velocity

P-wave velocity in marine sediments is influenced, among other things, by changes in lithology, bulk density, porosity, lithostatic pressure, degree of fracturing, degree of consolidation and/or the presence of solid gas hydrate or free gas. Combined with density measurements, the *p*-wave velocity is often used to calculate acoustic

impedance (the product of density and acoustic velocity) in order to construct synthetic seismic profiles and to estimate the depth of seismic reflectors. *P*-wave velocity can be measured continuously on most available MSTs or MSCLs using a pair of transducers acting as transmitter and receiver. Earlier transducers were static and required the addition of fluid, generally water, between the transducers and the core liner. Acoustic rolling transducers were subsequently developed to ensure full contact with the liner and thus eliminate the requirement for a fluid. In this type of transducer, the center of frequency is around 230 kHz, with an accuracy of ~50 ns depending on core thickness and condition. As for gamma density, the *p*-wave transducer should be placed horizontally rather than vertically to minimize possible sediment voids inside the liner due to gravity in whole cores.

2.4. Color Reflectance

Color reflectance is also one of the parameters generally measured on long cores immediately after splitting. A hand-held spectrophotometer with a 3-, 4- or 8-mm aperture is generally used to measure the percent diffuse reflectance of a known light source from the sediment surface with wavelengths ranging in most cases from 400 and 700 nm (visible spectrum) at 10 nm increments. Other systems such as the one developed at Oregon State University (see below) allow measurements over a wider set of wavelengths (250–950 nm). Using the first derivative of the reflectance spectrum, it is possible to derive information on sediment mineralogy such as the presence and concentration of iron oxides such as hematite and goethite (e.g., Deaton & Baslam, 1991; Balsam & Deaton, 1991; Balsam, Damuth, & Schneider, 1997). Empirical relationships between measured geochemical parameters and color parameters, such as L^* (lightness, see below), have been derived which can be used as high-resolution geochemical proxies (e.g., Mix, Harris, & Janecek, 1995; Weber, 1998; Ortiz, Mix, Harris, & O'Connell, 1999). Reflectance data can also be converted into the widely used *Commission Internationale de l'Éclairage* (CIE) L^*, a^* and b^* color space (Nederbragt & Thurow, 2004; see also Berns, 2000, for a comprehensive discussion of color systems). L^* ranges from 0 (black) to 100 (white), whereas a^* and b^* range from +60 (red) to −60 (green) and from +60 (yellow) to −60 (blue), respectively. L^* is widely used to highlight changes in carbonate or organic carbon contents (e.g., Mix et al., 1995; Ortiz et al., 1999; Peterson, Haug, Hughen, & Röhl, 2000; St-Onge, Mulder, Piper, Hillaire-Marcel, & Stoner, 2004), whereas variations in the a^* value are often associated with changes in the concentration of red minerals such as hematite (e.g., Helmke, Schulz, & Bauch, 2002). Variations in the b^* value of anoxic sediments have been reported to closely follow variations in diatom and organic matter contents (Debret et al., 2006). Downcore variations in reflectance-derived data have also been used for stratigraphic or correlation purposes (e.g., Mix, Rugh, Pisias, Veirs, & Leg, 1992; Peterson et al., 2000). Automated color reflectance measurements are now also possible with, for instance, the GEOTEK MSCL (Figure 1) or other systems such as the Oregon State University split-core analysis track (SCAT; Mix et al., 1992, 1995; Harris, Mix, & King, 1997; Ortiz et al., 1999). Several instruments have been used by the paleoceanographic community for diffuse reflectance measurements. For instance, a

few papers have discussed the use of the hand-held X-Rite Colortron (Andrews & Freeman, 1996; Boyle, 1997; Keigwin & Pickart, 1999), whereas most papers discuss the use of the more expensive Minolta hand-held spectrophotometers (e.g., Chapman & Shackleton, 2000; Ortiz & Rack, 1999 and references therein). Finally, color reflectance measurements can be correlated with results obtained using conventional tools for color description such as the Munsell chart.

2.5. Natural Gamma Radiation

Natural gamma-ray spectrometry allows estimation of elemental concentrations of K, U and Th using gamma emissions of their radioactive isotopes ^{40}K, as well as the ^{238}U and ^{232}Th series. These can be estimated by total counts or gamma spectra detected with two or more NaI scintillators and photomultiplier tubes. These detectors can be fully integrated, for instance, on the GEOTEK MSCL to perform continuous measurements (Figure 1). However, the time needed to obtain sufficient and acceptable counts is rather large compared to other measurements (Blum, Rabaute, Gaudon, & Allan, 1997), which limits the usefulness of the technique for continuous logging of sediment cores for paleoceanographic purposes. In addition, the spatial resolution of the measurements is rather low, depending in part on the NaI crystal diameter, which is generally ~5–8 cm.

3. Continuous Millimeter- to Micrometer-Scale Measurements of Physical Properties

3.1. Digital Core Imaging

High quality photographs of sediment cores can be used to image, quantify, and archive sedimentological changes in marine sediment cores. One of the goals of this approach is to capture variations in sediment color and texture before oxidization of the sediment surface takes place. Consequently, photographs are taken immediately after core splitting. Until recently, most core photographs were taken on conventional film, making this approach expensive, time consuming and difficult to combine with other continuous measurements performed onboard or onshore. High quality digital cameras are now much less expensive and hence extensively used to photograph sediment cores. Unfortunately, the process is still difficult and time consuming, in part because lighting is often inadequate and further image processing is necessary. In addition, images thus obtained cannot be used effectively for direct comparison with other continuous measurements. Two commercially available systems have recently solved some of these problems: the GEOTEK Geoscan III line-scan camera and the Smartcube smartCIS camera image scanner.

The Smartcube smartCIS camera image scanner consists of an 8.2 megapixels Canon EOS 20D digital camera mounted on a moving frame equipped with lights (Figure 3). Small electric motors control both vertical and horizontal movement of the camera. Picture taking and camera movement are controlled and recorded using

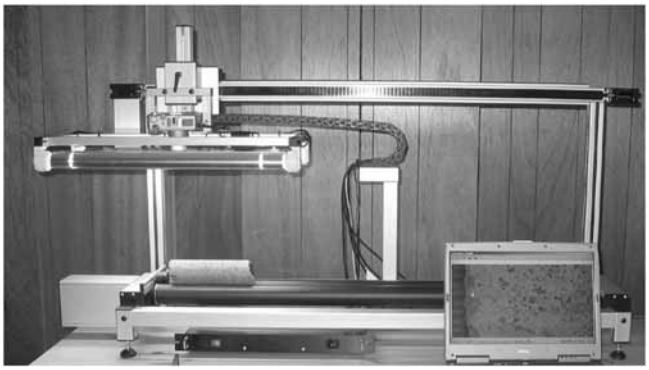

Figure 3 **Smartcube smartCIS camera image scanner. In this figure, the digital image of a whole rock core was acquired, unrolled and displayed on the companion laptop. Image modified with permission from http://www.smartcube.de/indexeng.htm**

a PC, and the companion software allows continuous reconstruction of an image of a core section not more than 1.5 m in length at a maximum pixel resolution of 33 μm (50 mm lens for 30–75 mm core diameters). For larger core diameters, the maximum pixel resolution is 63 μm (35 mm lens for 30–144 mm core diameters). One novel feature of this instrument is its ability to photograph whole rock cores by rotating the core, then "unrolling" the images using the software.

The Geoscan III line-scan camera is one of the latest improvements in sensors developed by GEOTEK and integrated into their automated MSCL (Figure 1). The setup consists of three individual interference filters placed in front of three 2048 Charge Coupled Device (CCD) line arrays inside the camera, one for each RGB color (red, green and blue). When properly calibrated, the resulting images can also be analyzed in terms of the three color arrays, providing downcore quantitative values of color variability (e.g., Moy, Seltzer, Rodbell, & Anderson, 2002; Nederbragt & Thurow, 2004). The standard instrument design allows the acquisition of images with a 50-μm pixel size on cores up to 10 cm wide. Pixel sizes down to 20 μm can be achieved, but for most routine applications, a 100 μm pixel size seems most practical (P. Schultheiss, personal communication, 2006). As with the Smartcube smartCIS camera image scanner, the GEOTEK MSCL can also be equipped with a new circumferential core imaging system, allowing imaging of the surface of a bare, round, whole rock core and unrolling of the resulting image to produce a complete 360° image. This makes it possible to look at geological structures and determine dip angles. A summary of the issues associated with digital core imaging is provided in Francus (2004).

3.2. Digital X-Ray Systems

X-ray radiography is a technique based on differential travel of X-rays through sediment (Bouma, 1969). During this travel, the incident X-ray beam is attenuated by various phenomena including absorption and scattering. The dominant control on beam attenuation is bulk sediment density (Holyer, Young, Sandidge, & Briggs,

1996; Jackson, Briggs, & Flint, 1996), which is in turn affected by parameters such as grain size and lithology, including carbonate and silica contents. Beam attenuation can also be affected by physical parameters such as changes in water content, compaction and porosity. The gray scale intensity of X-ray images is proportional to X-ray attenuation. Consequently, these images primarily reflect sediment density and, in theory, provide a first order picture of downcore grain size variations. However, gray level curve variations must be properly calibrated (refer to the Oregon State University system, below) or interpreted using complementary mineralogical (e.g., carbonate contents) and grain-size data obtained from the sediments using conventional sedimentological analysis methods.

Until recently, X-radiographs of marine sediment cores or slabs were obtained on conventional chemical film, making the process not only relatively time consuming but also expensive and inconvenient for image postprocessing, which required at least one additional step consisting in digitizing the film (e.g., Principato, 2004). In contrast, digital X-ray images of sediment slabs or cores can be taken quickly both onshore and onboard, and their use in image analysis is direct and straightforward. Digital X-radiography can mainly be used for high-resolution sedimentological analysis (millimeter- to centimeter-scale), but can also be used effectively for assessing bioturbation. In sedimentology, its main applications are for identifying sedimentary facies and sequences at the process scale (individual sequence) and constraining the evolution of sequences over time (nature, size, frequency, rhythms and cycles). This method is also very useful for identifying laminae or other sedimentary structures that may be unrecognizable to the naked eye, for detecting the base and top boundaries in a sedimentary sequence, for characterizing grain size trends within a given sequence, for downcore high-resolution analysis of textural and structural variations, for facies differentiation and for detecting facies changes and assessing sampling quality and position. For instance, extracted high-resolution gray curves (see Section 4.3) may be readily correlated with other physical parameters (color, gamma density, magnetic susceptibility, grain size changes) and other cores. What follows is a brief overview of some available onboard and onshore digital X-ray systems, which may be used for rapid measurement of marine cores.

The digital X-ray imaging system developed at the Université Bordeaux 1 (SCOPIX) consists of conventional X-ray equipment combined with a new radioscopy instrument developed by the Cegelec Company (Migeon, Weber, Faugères, & Saint-Paul, 1999; Lofi & Weber, 2001). The lead box (0.8 m wide, 0.8 m long, and 1.2 m high) is built on a base equipped with two motorized lateral sleeves to move the sediment samples (Figure 4). The upper part of the box contains the X-ray source (160 kV, 19 mA) with a water-cooling system. X-rays pass through the sediment and the resulting signal is amplified. Originally, X-rays were recorded by a high-resolution CCD camera (756 × 581 pixels) with a pixel size of 0.21 mm. This camera was used to collect the sample images shown in Figures 14 and 15. The system was recently improved with the addition of a 4096 gray level Hamamatsu ORCA camera (1,280 × 1,024 pixels). The signal recorded by the camera is transferred to a computer, which converts it into gray level values. High-resolution gray level images are acquired and reconstructed using one software, while another

Figure 4 Photograph of the complete SCOPIX system showing the X-ray lead-protected box and the two sleeves on each side.

software is used for image processing (Migeon et al., 1999). The acquisition software records basic information about the core, whereas the processing software is used to display downcore X-ray intensity logs (gray scale values) including the mean, median, minimum and maximum values and standard deviations. Further processing of the images has been extensively described by Lofi and Weber (2001), and may include the use of several numerical filters and extractions. Filter parameters and procedure vary depending on whether the purpose is to enhance sequence boundaries or highlight internal sedimentary structures. For further examples of applications of conventional X-rays image analysis, see Francus (2004) and references therein.

Although SCOPIX measurements can be made on u-channels, split or whole cores, they are generally performed on aluminum slabs or trays. The slabs are extracted continuously from split cores using an electro-osmotic core cutter (Chmelick, 1967). Conventional slab dimensions are <7 cm wide and <1.5 m long. A thickness of $\sim$1 cm provides the best results. Thinner slabs would yield higher precision, but would be very difficult to subsample. Uniform slab thickness prevents attenuation variations due to thickness changes.

Shipboard digital X-ray systems have several key advantages over onshore systems. Firstly, they allow rapid visualization of sediment cores prior to splitting, which may facilitate operational decision making at sea. For instance, they may help in determining whether a specific sedimentary target or stratigraphic interval was successfully cored. Secondly, they help constrain splitting, subsampling, and even logging strategies. Thirdly, archived X-ray images taken onboard reflect the pristine state of the sediments prior to any changes related to transport and splitting,

such as compaction and deformation. Until recently, no commercial digital system was readily available. However, GEOTEK can now produce an X-ray system that is fully compatible with the existing range of nondestructive measurements for the MSCL. This system will provide continuous high-resolution digital X-ray images of whole or split cores, at a resolution of approximately 100–150 μm. The images will be viewed with other MSCL data, and a preview mode will be available for real-time viewing. A prototype of this X-ray system was successfully used on pressure cores by GEOTEK personnel during IODP Expedition 311 and revealed fine scale gas hydrate structures (P. Schultheiss, personal communication, 2006).

Another more portable system was recently developed by Dr. Robert Wheatcroft at Oregon State University (Figure 5). Among other features, this system uses

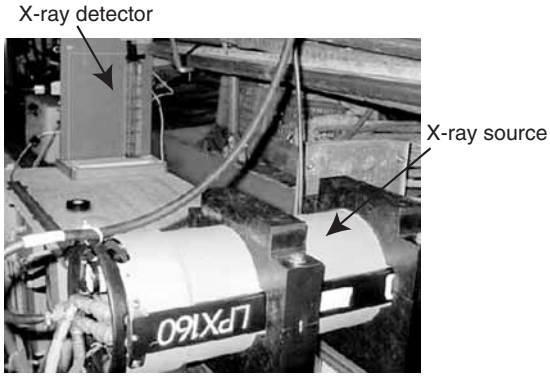

Figure 5 Oregon State University (OSU) portable shipboard digital X-ray system onboard the *R/V Garcia del Cid*. The X-ray source and detector are shown.

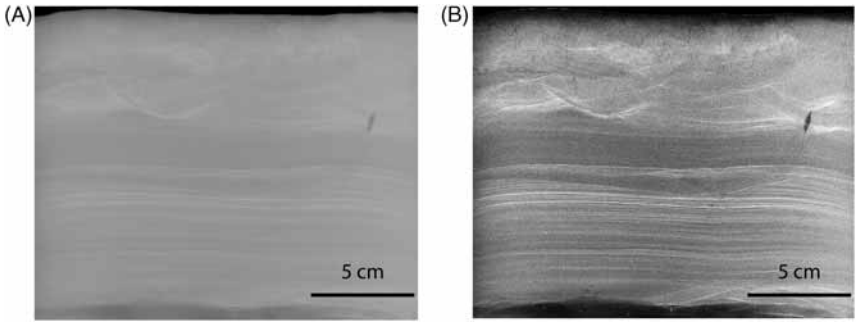

Figure 6 Example of a digital X-radiograph (negative) taken from a box core sampled in an 8-m silty sand site off the Po River using the OSU shipboard system. (A) Raw image; (B) processed image. The original bit depth was 12. The processed image is the result of applying a sharpening algorithm, followed by contrast normalization (see Wheatcroft et al., 2006 for examples). Note the very fine laminations present in the core as well as the small pelecypod in living position in the middle right.

a dpiX Flashscan 30 imager X-ray detector that can capture 29.3 × 40.6 cm images at 12-bit depth (i.e., 4,096 gray levels) and 127-μm pixel size (Figure 6). In addition, in each image, 16 sections of different glass thicknesses make it possible to calibrate image brightness to absolute density values, allowing the extraction of quantitative information. This system was recently used to identify newly deposited and highly porous sediments (Stevens, Wheatcroft, & Wiberg, 2007), as well as to map and identify flood deposits (Wheatcroft, Stevens, Hunt, & Milligan, 2006). Combined with image analysis, the system was very effective at rapidly identifying the 2000 Po River flood deposit at 33 stations, from box cores collected near the Po River Delta, Italy.

3.3. Computerized Coaxial Tomography (CAT-Scan)

Computerized axial tomography (CAT-scan) allows rapid visualization of both longitudinal and traverse sections of sediment cores. The CAT-scan method (Figure 7) uses a pixel intensity scale to quantify and map X-ray attenuation coefficients of the analyzed object on longitudinal (topogram) or transverse (tomogram) images. The resulting images are displayed in gray scale, darker and lighter zones representing lower and higher X-ray attenuation, respectively. Gray scale values are expressed as CT numbers or Hounsfield units, obtained by comparing the attenuation coefficient (μ) to that of water (μ_w):

$$\text{CT(Hounsfield units)} = (\mu/\mu_w - 1) \times 1000 \quad (1)$$

A CT number is a complex unit related to sediment bulk density, mineralogy, as well as porosity (e.g., Boespflug, Long, & Occhietti, 1995; Crémer, Long, Desrosiers, de Montety, & Locat, 2002). This nondestructive and very high-resolution method

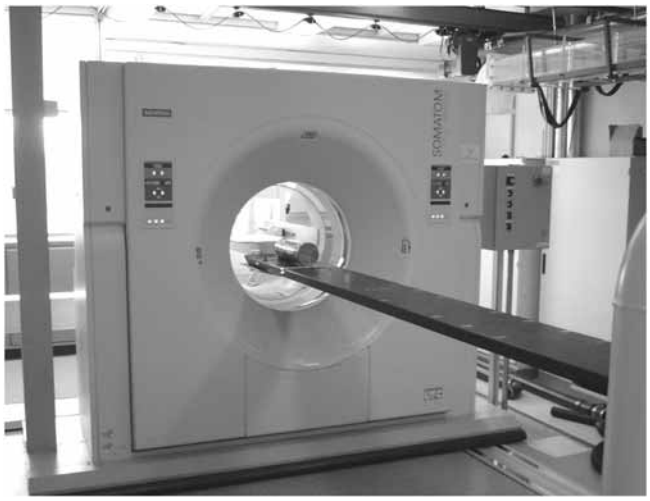

Figure 7 Siemens Somatom Volume Access CAT-scan at the *Laboratoire Multidisciplinaire de Scanographie de Québec (LMSQ).*

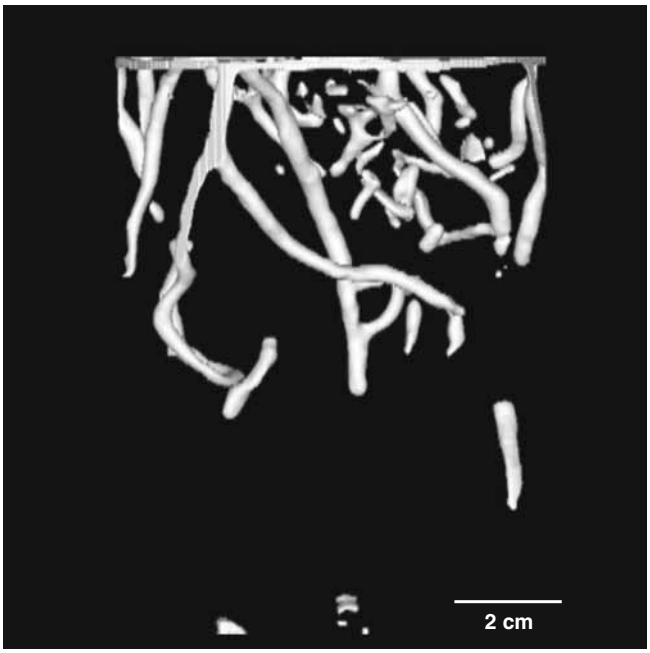

Figure 8 3D reconstruction of biogenic structures in a box core from Baie des Chaleur Bay, Eastern Canada. The structures (*Nereis* worm tubes) were highlighted by selecting a specific range of tomographic intensities using the OsiriX freeware (see Dufour et al., 2005 for method details).

(~0.1–1 mm) has been used to identify sedimentary structures (Champanhet, Durand, Long, & Laberye, 1989; Holler & Kögler, 1990; Orsi, Edwards, & Anderson, 1994), determine sediment deposition mode (Crémer et al., 2002), characterize the benthic community (Mermillod-Blondin et al., 2003; Michaud et al., 2003), establish a high-resolution stratigraphy (Boespflug et al., 1995), evaluate the physical properties of sediments (Wellington & Vinegar, 1987; Kantzas, Marentette, & Jha, 1992; Orsi et al., 1994; Amos, Sutherland, Radzijewski, & Doucette, 1996) and even visualize biogenic structures in sediment cores in 3D (Figure 8, see Dufour et al., 2005 for more details). For more examples of CAT-scan applications in geoscience, refer to Mees, Swennen, Van Geet, and Jacobs (2003), as well as Duliu (1999) and Ketcham and Carlson (2001). Section 4.3 of this chapter illustrates the usefulness of CAT-scan as a paleoceanographic tool.

3.4. Micro X-Ray Fluorescence Spectrometry

A new generation of core logging instruments is currently being used in the paleoceanographic community to perform downcore mm- and even μm-scale measurements on split cores. These new instruments use micro X-ray fluorescence spectrometry to estimate continuously the elemental composition and concentration of elements from Si to U. In these instruments, an intense X-ray beam is used

to irradiate the sediment surface and thus enable X-ray fluorescence analysis. Both commercially available models (Cox Analytical Systems Itrax and Avaatech XRF Core scanner) may also be combined with a line-scan camera to acquire a high-resolution RGB image of the analyzed core. The ITRAX also allows acquisition of a digital X-ray image along the center of the core for a 20 mm-wide area at a pixel size as small as 25 μm. X-ray fluorescence spectrometry can be performed at a maximum resolution of 100 μm and 1 mm, respectively, for the ITRAX and Core scanner.

Detected elements and detection limits depend upon the composition of the anode in the tube used to produce the emitted X-rays, acquisition time and the atomic number of the element being detected. For instance, using a molybdenum tube, a wide range of elements can be detected from Al to U. Detection limits for lighter elements, such as Al and Si, are much higher (in the order of a few percent) and therefore require much longer counting time. Heavier elements such as Fe or Rb can be detected in trace amounts (on the order of a few tens of ppm). For each data point, a dispersive energy spectrum is acquired and evaluated. Energy peaks for each element in the spectrum can be identified and measured. Calibration procedures are available which compare a sample of known and/or certified composition with the analyzed sample in order to produce results as concentration rather than counts per second or peak surface area. However, numerous factors such as the presence of organic matter, porosity variations, water content, grain size, crystallinity and sample topography may have an impact on the production and detection of fluorescent radiation. Caution must therefore be exercised in using such quantitative results, because the nature and physical properties of the standard are never identical to those of the sample analyzed. Elemental concentrations and ratios do however provide extremely valuable and useful information.

In paleoceanography, X-ray microfluorescence is used for two main purposes: (1) the study of sedimentation processes and (2) the study of forcing parameters affecting sedimentation (and thus the development of paleoclimatic proxies). As with X-ray analysis, this methodology can also constitute a tool for preliminary investigations and for the selection of specific intervals over which to perform conventional sedimentological analysis. In clastic sedimentology, the comparison of elements typical of the siliciclastic fraction (Al, Ti, Fe, etc.) and the biogenic fraction (Ca, Sr, etc.) can help in distinguishing periods of increased terrigeneous input into the deep oceans. For instance, in a Late Quaternary core collected off the Channel Sea, in the Armorican Deep Sea Turbidite System, both microfluorescence-X and digital X-rays measurements were used to determine changes in sedimentation type (Figure 9, Zaragosi et al., 2006). During isotopic stage 2, the Ti/Sr ratio is high and the sediment is laminated, both observations suggesting frequent and important terrigeneous inputs, probably by turbidity currents, whereas a decrease of both the Ti/Sr ratio and the number of laminae during isotopic stage 1 and, in particular, during the Holocene suggests a strongly reduced terrigeneous sediment source. The very high Ti/Sr ratio values observed between 15 and 13.8 kyr BP also clearly reflect the proximal deglacial sedimentation phase of the British Ice Sheet. This example highlights the fact that it is possible to constrain

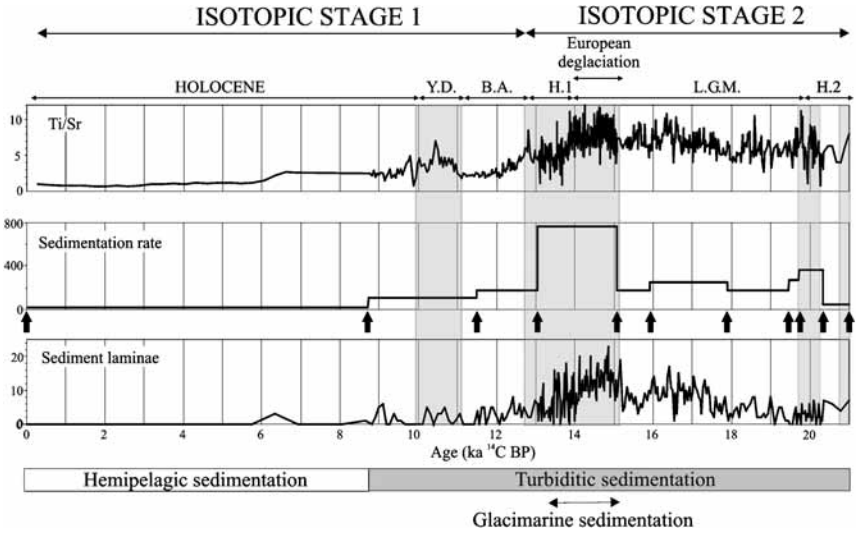

Figure 9 **Microfluorescence-X (Avaatech XRF core scanner) measurements (Ti/Sr ratio) processed at the University of Bremen, and laminae count data obtained with the digital X-ray device at Université Bordeaux 1 (SCOPIX) on core MD03-2690. Modified with permission from Zaragosi et al. (2006).**

sedimentation type (hemipelagic, turbiditic and glaciomarine) using only non-destructive measurements (digital X-ray and microfluorescence-X).

Microfluorescence-X has also been used for paleoceanographic purposes on cores collected off of Antarctica (Hepp, Mörz, & Grützner, 2006; Grützner, Hillenbrand, & Rebesco, 2005), Africa (Kuhlmann, Freudenthal, Helmke, & Meggers, 2004a, 2004b; Adgebie, Schneider, Röhl, & Wefer, 2003; Bozzano, Kuhlmann, & Alonso, 2002; Stuut et al., 2002a); and Chile (Lamy, Hebbeln, Röhl, & Wefer, 2001), in the Black Sea (Bahr, Lamy, Arz, Kuhlmann, & Wefer, 2005), Red Sea (Arz, Pätzold, Müller, & Moammar, 2003), Mediterranean Sea (Rothwell, Hoogakker, Thomson, & Croudace, 2006; Thomson, Croudace, & Rothwell, 2006), Gulf of California (Cheshire, Thurow, & Nederbragt, 2005), Nordic seas (Helmke, Bauch, Röhl, & Mazaud, 2005), North Pacific (Jaccard et al., 2005), SE Atlantic (Westerhold, Bickert, & Röhl, 2005; West, Jansen, & Stuut, 2004; Stuut, Prins, & Jansen, 2002b; Vidal, Bickert, Wefer, & Röhl, 2002), Equatorial Atlantic (Funk, von Dobeneck, & von Reitz, 2004a; Röhl, Brinkhuis, Fuller, Schellenberg, Stickley, & illiams, 2004b), tropical Atlantic (Arz, Gerhardt, Pätzold, & Röhl, 2001) and Southern Ocean (Röhl, Brinkhuis, & Fuller, 2004; Röhl et al., 2004; Andres, Bernasconi, McKenzie, & Röhl, 2003). This wealth of recent papers clearly highlights the increasing use of this nondestructive high-resolution method in paleoceanographic research. Furthermore, we have recently successfully employed the ITRAX on u-channel samples to generate a continuous dataset including high-resolution RGB and X-ray images as well as the concentration of several important elements in paleomagnetic studies, such as Ca, Ti, and Fe (Figure 10). These data, along with images and X-ray measurements, will be useful for the interpretation of downcore magnetic properties and to assess

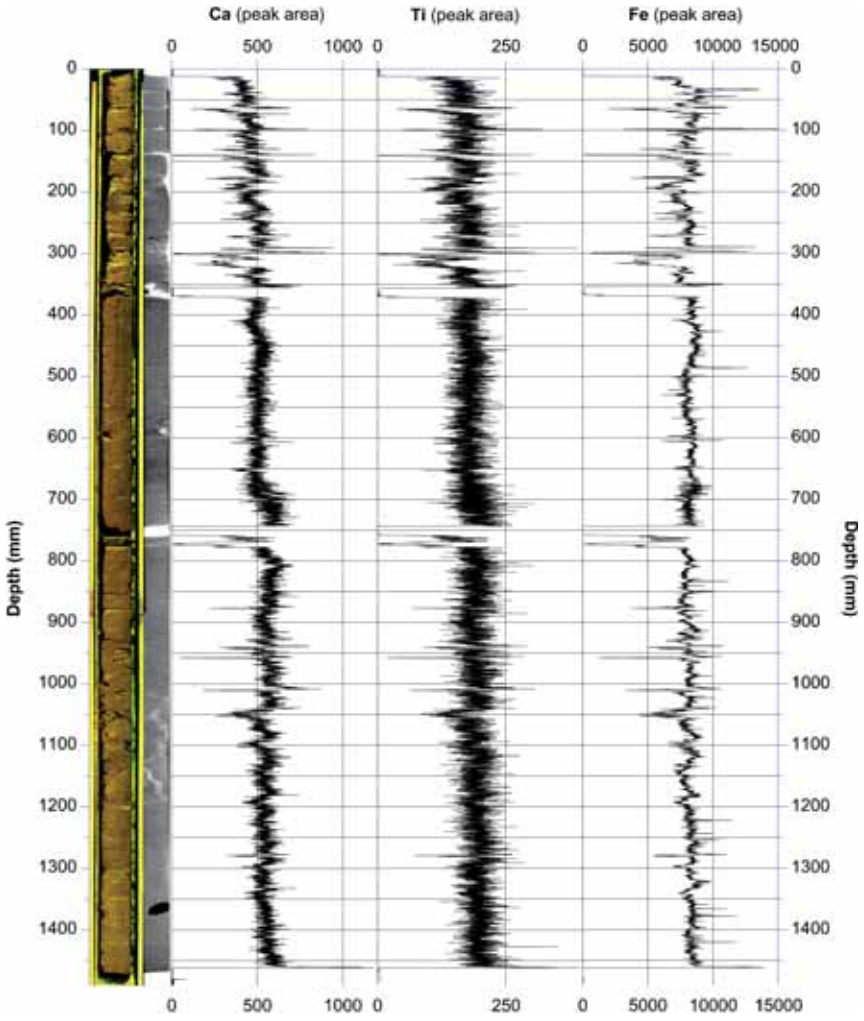

Figure 10 RGB image, digital X-ray and relative Ca, Ti and Fe counts obtained using the ITRAX core scanner on a u-channel sampled in the upper section (0–150 cm) of core 2004–804–009 from Lancaster Sound, Eastern Canadian Arctic. The downcore stability of the profiles suggests relatively low variability in the concentration of magnetic minerals, an essential criterion for paleomagnetic relative paleointensity determinations. The images also highlight sampling and coring artifacts.

the influence of coring and/or subsampling deformations on the paleomagnetic signal, because these different types of measurements can all be performed on the same u-channels. In another example (Figure 11) on fjord sediments collected in Saanich Inlet, off of Vancouver Island (British Columbia, Canada), ITRAX data clearly delineate varved sediments and were used to determine varve counts. For a detailed description of the ITRAX system, the reader is referred to Croudace, Rindby, and Rothwell (2006).

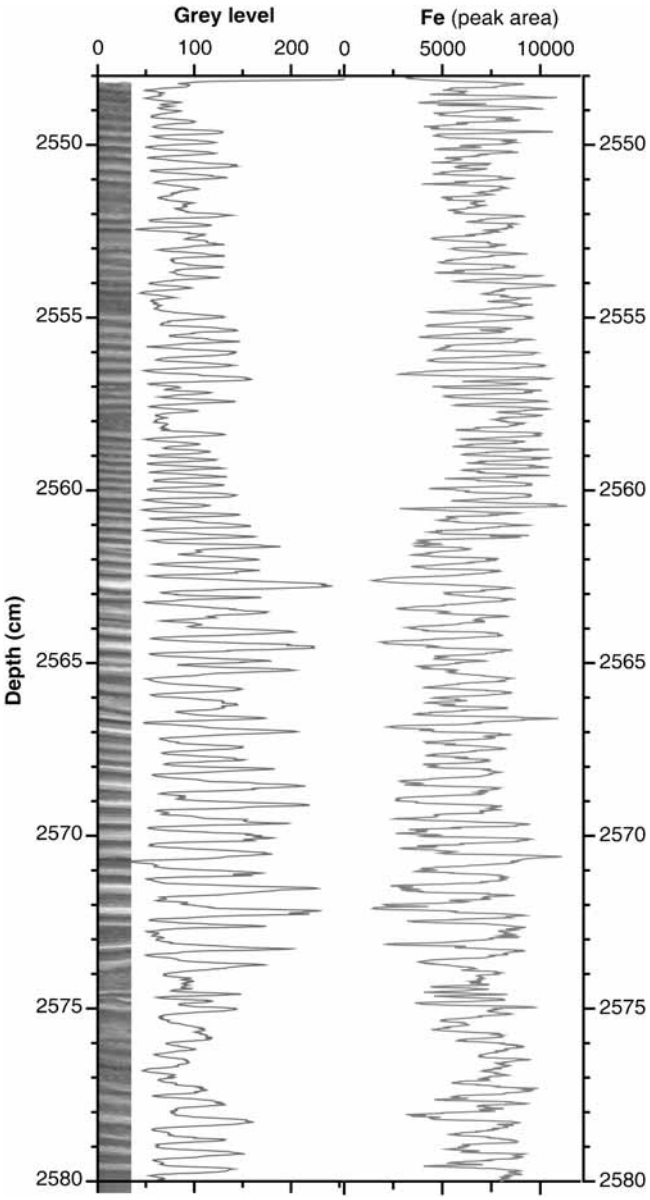

Figure 11 Digital X-ray, gray level values and relative Fe counts obtained using the ITRAX core scanner on a u-channel sampled in section XVIII (2,548–2,580 cm depth) of core MD02-2490 from Saanich Inlet, off of Vancouver Island. Each lamination is clearly resolved in both the radiograph and the Fe profile; these plots along the 32 cm long section each contain 3,200 data points.

3.5. Magnetic Resonance Imaging (MRI) and Nuclear Magnetic Resonance (NMR)

As pointed out by Rack (1998), MRI has the potential to become a very useful technique for marine sediment imaging, especially for 2D and 3D imaging of sediment cores. MRI calls upon the principles of NMR to generate images of a scanned object. Originally, this technique was called nuclear magnetic resonance imaging (NMRI), but the word "nuclear" was dropped from the acronym to remove any negative connotation. The MRI technique is used to produce images of nuclear spin density or magnetic resonance relaxation times, chemical shifts and fluid flow velocity (e.g., Ortiz and Rack, 1999). MRI has been used in petrographic studies to determine porosity, pore size distribution and/or flow and diffusion properties of various porous media such as rocks (e.g., Attard, McDonald, Roberts, & Taylor, 1994; Davies, Hardwick, Roberts, Spowage, & Packer, 1994; Mansfield & Issa, 1996; Baumann, Petsch, Fesl, & Niessner, 2002; Gingras, MacMillan, Balcom, Saunders, & Pemberton, 2002; Marica et al., 2006; Chen, Rack, & Balcom, 2006). Similarly, Kleinberg and Griffin (2005) successfully applied NMR to the quantification of the pore scale distribution of ice and the hydraulic permeability of sediments from Alaskan permafrost cores, using the Schlumberger Combinable Magnetic Resonance (CMR) tool on 15 cm of every 1-m section of core from a 438-m deep borehole. These authors also used a nearly identical NRM tool to characterize the borehole itself, allowing direct core/borehole comparison. To our knowledge, however, the study by Rack, Balcom, MacGregor, and Armstrong (1997) is the only one in which MRI was successfully used continuously to image cored sediments. In this study, the transition from Lake Agassiz proglacial to Lake Winnipeg lacustrine sediments was imaged from a core collected in Lake Winnipeg, Canada (Figure 12), and the authors showed that the resulting MRI images reflected variations in magnetic susceptibility and porosity.

3.6. Confocal Macroscopy and Microscopy

Another promising method is confocal macro- or microscopy. This method uses a confocal scanning laser (Dixon, Damaskinos, Ribes, & Beesley, 1995; Ribes, Damaskinos, & Dixon, 1995; Ribes, Damaskinos, Tiedje, Dixon, & Brodie, 1996; Dixon & Damaskinos, 1998) to image specimens ranging from 200×200 μm up to 7.5×7.5 cm in less than 10 s, either in reflected light or photoluminescence. In this technique, a laser beam is focused into a small aperture so as to limit the depth of field to a single plane. The resulting image is then constructed by combining several images obtained for different surface planes. In macroscopic mode, the images have a lateral resolution of 10 μm, whereas in microscopic mode, the lateral resolution is approximately 1–2 μm (Ribes et al., 2000). For example, Ribes et al. (1998) and Rack et al. (1998) successfully imaged several sections of sediment cores in both macroscopic and microscopic modes. More recently, Ribes et al.

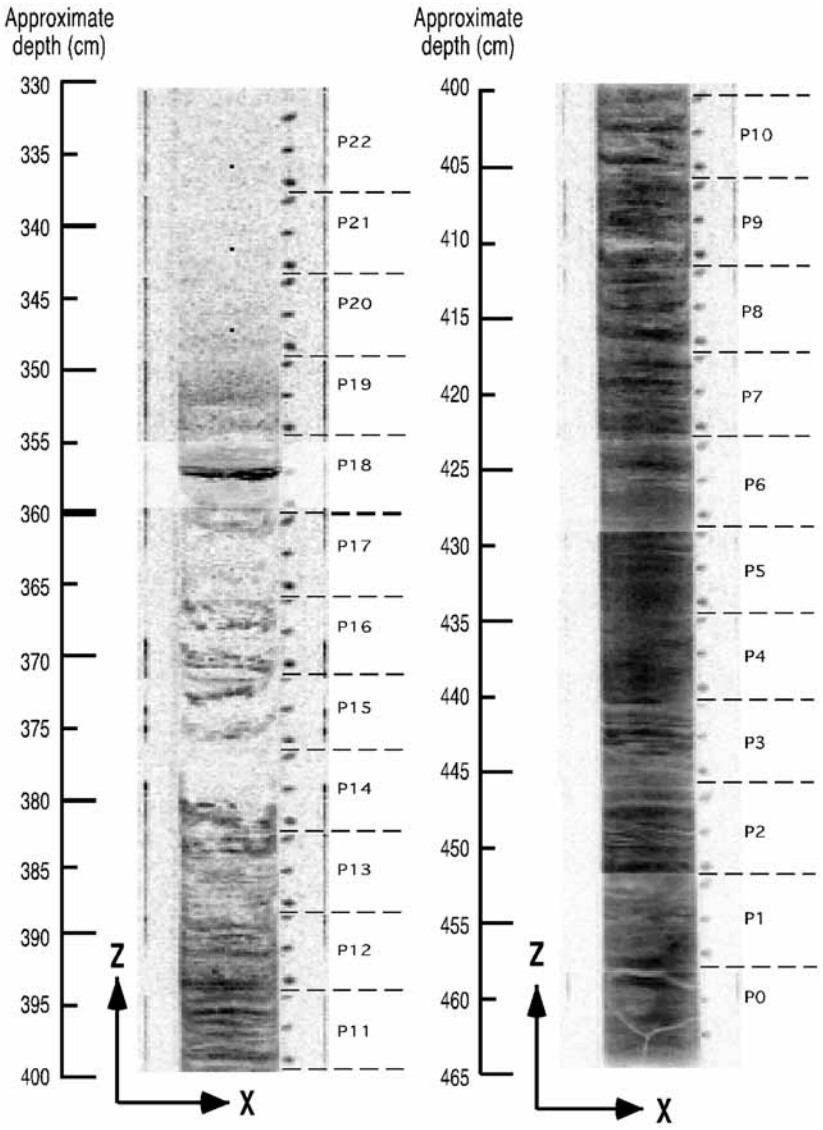

Figure 12 Magnetic Resonance Imaging (MRI) images of Section 4 of core *Namao* 94–900–122a (313–465 cm) from Lake Winnipeg, Canada. The images were obtained using the Single-Point, Ramped Imaging with T_1 Enhancement (SPRITE) technique. Individual SPRITE images are ~5 cm in length (P0 to P22). Dark bands reflect high signal intensity (associated with low porosity and/or high magnetic susceptibility), whereas lighter bands reflect lower intensity (associated with high porosity and low magnetic susceptibility). From Rack et al. (1997), with permission.

(2000) illustrated the usefulness of the method for imaging speleothems at both low and high resolution (Figure 13), allowing the clear identification of annual laminations, which may constitute a possible analogue to finely laminated marine sediments.

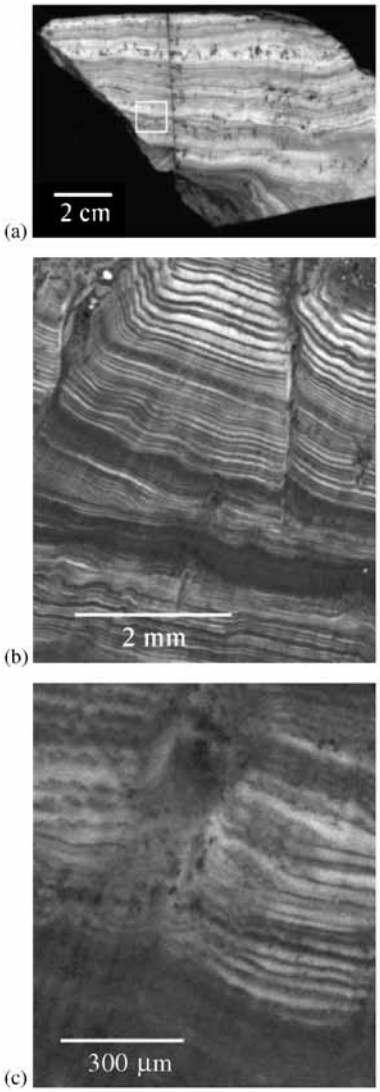

Figure 13 Photoluminescence images of speleothem specimen B104 taken with a high-resolution confocal scanning laser macroscope. (A) Overall image of the speleothem; (B and C) successive enlargements of the area highlighted in A. Modified with permission from Ribes et al. (2000).

4. Recent Applications of Continuous Centimeter- to Millimeter-Scale Physical Properties of Marine Sediments

The last section of this chapter describes the use of continuous centimeter- to millimeter-scale measurements of physical properties of marine sediments and their

combination with other more traditional methods to (1) identify and characterize turbidites, (2) identify and determine the trigger mechanism for RDL from the Saguenay Fjord, Québec, and (3) develop a seasonal- to millennial-scale paleoceanographic tool.

4.1. Use of Digital X-Ray to Rapidly Identify Turbidites in Marine Sediments

In 2000, a 33-cm long Barnett interface gravity core was taken in the talweg of the Capbreton Canyon (southern Bay of Biscay), at a water depth of 647 m. Digital X-ray (SCOPIX) analysis of the gravity core allowed the identification of a succession of sedimentary facies which can be interpreted as three superimposed sequences separated by hemipelagic interfaces (Mulder, Weber, Anschutz, Jorissen, & Jouanneau, 2001c; Figure 14). The two buried interfaces were paleo-seafloors and the upper interface forming the top of the core was the present-day seafloor. The top sequence showed a classical facies succession forming a turbidite sequence as defined by Bouma (1962). Micro-grain size analyses showed the classical normal grading expected for a surge-like waning flow. To validate the positional accuracy of samples used for grain size analysis, the core was once again X-radiographed after sampling.

Measurements of short-lived radiogenic isotopes provided evidence for the recent deposition of this turbidite. Values of excess ^{210}Pb (half-life = 22.3 yr) are very high,

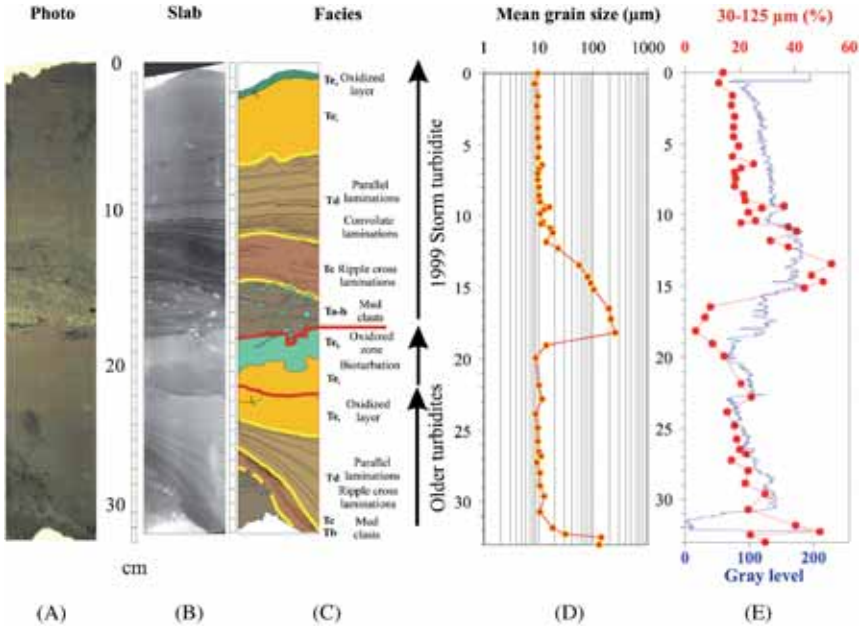

Figure 14 Core K showing the 1999 turbidite deposited in Capbreton Canyon, France. (A) Photograph, (B) X-ray image (SCOPIX), (C) facies interpretation, (D) grain size distribution curve, and (E) extracted gray levels (from the X-ray image) and abundance of the 30–125 μm fraction. Modified with permission from Mulder et al. (2001c).

and values for the interfaces both above and below the turbidite fall in the same range, which suggests very recent deposition. Excess ^{234}Th (half-life = 24.1 days) values confirmed this interpretation. $^{234}Th_{exc}$ activity suggests that deposition occurred at most 6 months before sample counting (between 15/05/2000 and 02/06/2000), in the period between 05/12/1999 and 14/01/2000. During this period, the only event capable of triggering a turbulent surge was the violent "Martin" storm that hit the Bay of Biscay on December 27th, 1999. This turbulent surge could have been generated by three processes: (1) the transformation of a slide which originated at the head of Capbreton Canyon in response to excess interstitial pore pressure in the sediments resulting from 12-m high storm waves or exceptionally high swell, (2) the dissipation through the canyon of a 1–2 m high along-coast water bulge resulting from low barometric pressure, or (3) the increased coastal drift and shelf current intensities.

In the Var Canyon (Mediterranean Sea, French Riviera), digital X-ray analysis lead to the description of a new type of sedimentary sequence called hyperpycnite (Mulder, Migeon, Savoye, & Faugères, 2001a; Mulder, Migeon, Savoye, & Faugères, 2002; Figure 15). Hyperpycnites are sedimentary sequences deposited by turbulent flows generated at river mouths during floods, when the suspended

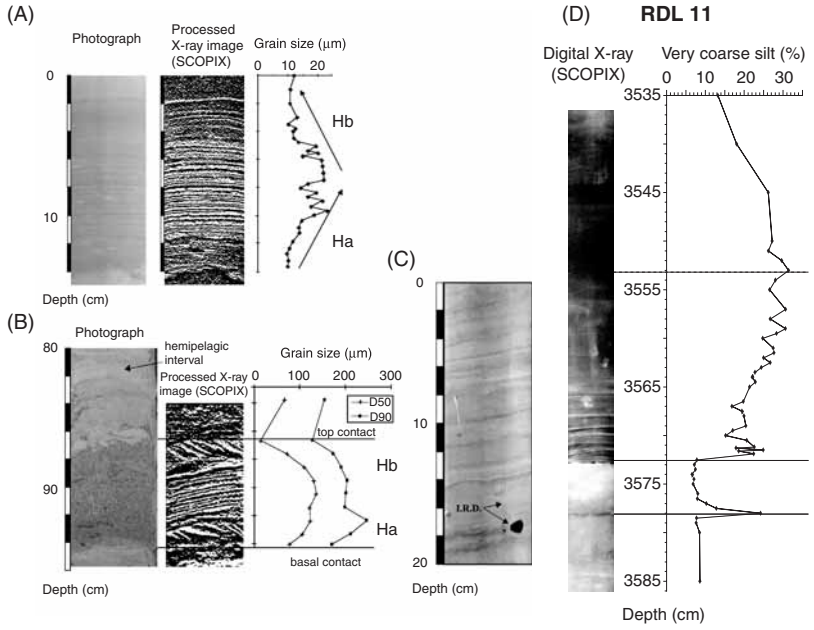

Figure 15 Examples of digital X-radiographed sequences: complete hyperpycnal turbidite sequence from the Var (A) and Zaire (B) turbidite systems. Note the superposition of coarsening upward unit Ha and fining upward unit Hb. (C) Finely laminated clays and silty clays from the northwestern Bay of Biscay associated with ice melting at the end of the last ice age, between 15–14.4 yr BP. I.R.D.: Ice-Rafted Detritus. (D) Base of the turbidite sequence of rapidly deposited layer 11 from the Saguenay Fjord, Eastern Canada. Modified with permission from Mulder, Syvitski, Migeon, Faugères, and Savoye (2003) and St-Onge et al. (2004).

sediment concentration in the fresh water is high enough for the density of river water and its suspended sediment to exceed that of seawater in the marine basin (hyperpycnal flow; Mulder & Syvitski, 1995). This sequence comprises two superposed units. The basal, coarsening upward unit corresponds to the waning part of the hyperpycnal flow deposited during the rising portion of the flood hydrograph at the river mouth (Mulder, Syvitski, & Skene, 1998). The top, fining upward unit corresponds to the waning part of the hyperpycnal flow deposited during the falling portion of the flood hydrograph at the river mouth. The peak grain size corresponds to the peak of the flood at the river mouth. Numerous internal erosive or sharp surfaces are observed within this sequence. The base surface can be erosive, sharp or transitional. The top surface is usually sharp or transitional. Digital X-ray images of such sequences in the Var Giant Sedimentary Levee (Migeon, 2000; Migeon et al., 2001; Mulder, Migeon, Savoye, & Jouanneau, 2001b) and in the Zaire deep-sea turbidite system (Migeon, 2000) clearly show this type of sequence (Figure 15). They show internal sedimentary structures, the most common of which are climbing ripples, which suggest a high sediment load. In addition, numerous intrasequence erosional or sharp contact surfaces may be present. For thick hyperpycnal sequences such as the 2.2-m thick, rapidly deposited layer 11 in the Saguenay Fjord, digital X-ray imaging reveals unexpected planar horizontal lamination in the basal (waxing) unit (Figure 15).

4.2. RDL in the Saguenay Fjord

Several natural disasters have struck the Saguenay Fjord over the last few centuries. These include the 1663 ($M \approx 7.0$) and 1988 ($M = 6$) earthquakes, the 1924 Kénogami and 1971 Saint-Jean-Vianney landslides and the catastrophic flood of 1996, which swept more than $15 \times 10^6\,m^3$ of sediment into the Saguenay Fjord (Lapointe, Secretan, Driscoll, Bergeron, & Leclerc, 1998). Previous studies have revealed the presence of thick sediment deposits associated with these events, varying from several centimeters to several meters in thickness, in the Baie des Ha!Ha! and inner basin of the Saguenay Fjord (Smith & Walton, 1980; Syvitski & Schafer, 1996; St-Onge & Hillaire-Marcel, 2001). These deposits generally consist of light gray homogenous silty clays that contrast sharply with the dark gray, bioturbated background sediments. In this section, we illustrate how high-resolution continuous measurements were used to image and/or identify RDL associated with historic and prehistoric catastrophic events during the last 7,200 cal yr BP. For instance, the 1996 flood layer is shown in Figure 16, in which the difference between the photograph and the CAT-scan image is clearly visible. This figure also clearly highlights the laminations and internal sedimentary structures of the flood layer. Similarly, CAT-scan images and photographs of the four core sections of a ~4 m piston core sampled in the northern arm of the Saguenay Fjord (Figure 17) clearly show the 1996 flood layer (e.g., St-Onge & Hillaire-Marcel, 2001; Urgeles, Locat, Lee, & Martin, 2002), the 1971 Saint-Jean-Vianney (e.g., Smith & Walton, 1980) and the 1924 Kénogami (e.g., Smith & Schafer, 1987) landslide layers, as well as the top part of the 1663 turbidite. In 1999, a 38 m-long Calypso piston core (core MD99-2222) was raised from the deepest part of the Saguenay Fjord inner basin in order to identify RDLs older than the 1663

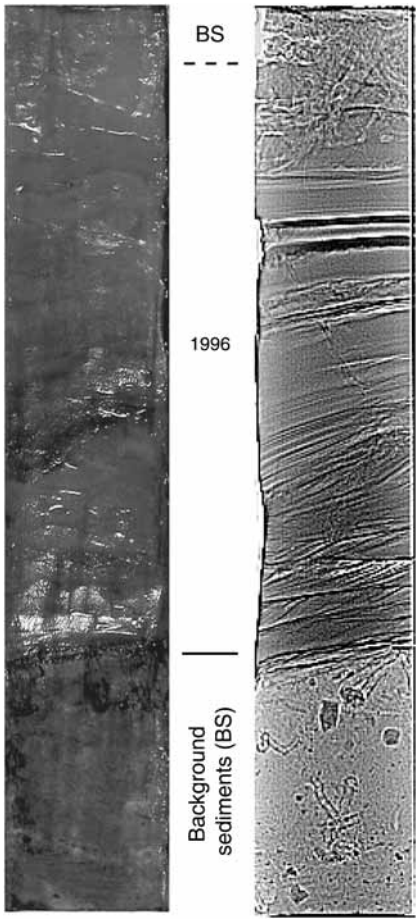

Figure 16 Digital photograph (left) and CAT-scan (right) of the 1996 Saguenay flood layer. The images were taken from a box core collected in the northern arm of the Saguenay Fjord. The push core is ~54 cm in length.

earthquake RDL. High-resolution physical (density, diffuse reflectance and digital X-radiography), magnetic (magnetic susceptibility and inclination), sedimentological (detailed description and grain size) and geochemical ($CaCO_3$) analyses revealed the presence of at least 14 RDLs, including a ~16-m thick layer associated with the 1663 AD earthquake (Figure 18). These RDLs are readily recognizable by their sharp and sandy bases, which are clearly visible on the digital X-rays images (Figure 15D) and highlighted by high density and magnetic susceptibility values. In addition, these layers are characterized by a light gray color, high $CaCO_3$ contents and low basal paleomagnetic inclinations, contrasting sharply with the dark gray bioturbated background sediments. The light gray color (higher L^* values) and the high $CaCO_3$ contents indicate the incorporation of reworked gray and slightly carbonated Laflamme Sea clays (St-Onge & Hillaire-Marcel, 2001), whereas the low paleomagnetic inclinations at the base of the RDLs indicate an energetic depositional process,

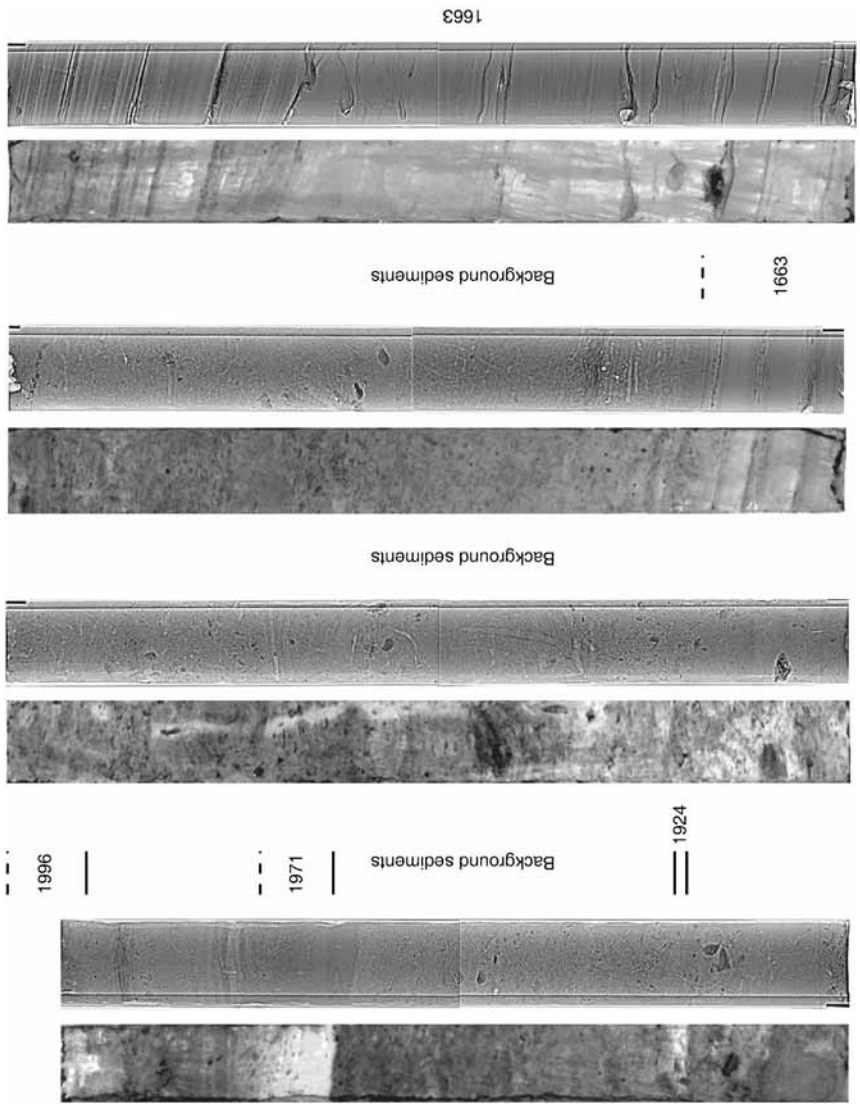

Figure 17 Digital photograph (left) and CAT-scan (right) of several historic rapidly deposited layers (RDLs) from the Saguenay Fjord. The images were taken from the four (~1 m) sections of a piston core collected in the northern arm of the Saguenay Fjord.

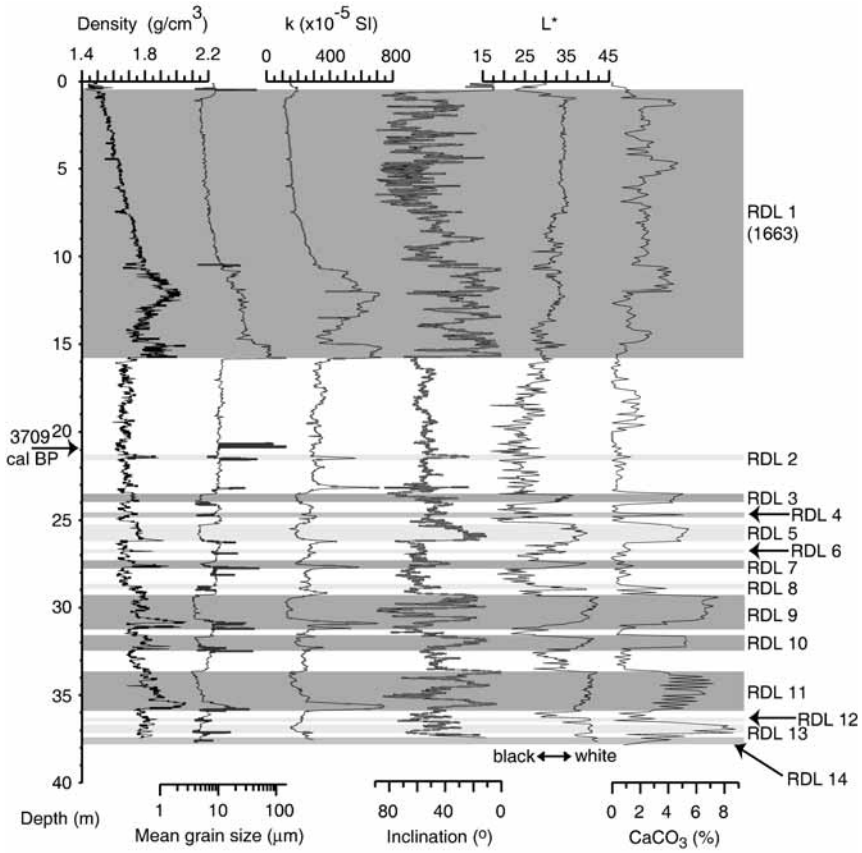

Figure 18 Physical properties of rapidly deposited layers (RDLs) in core MD99-2222. Gray zones correspond to RDLs. RDL 1 is associated with the 1663 AD earthquake. Bulk density and low field volumetric magnetic susceptibility (k) were measured using a GEOTEK MSCL onboard the *Marion Dufresne II*. L^* was measured using a CM-2002 Minolta hand-held spectrophotometer. Inclinations were calculated by principal component analysis using 4–10 alternating field (AF) demagnetization steps at peak fields of 10–80 mT, using a 2-G Enterprises model 755 cryogenic magnetometer at the University of California, Davis. The $CaCO_3$ content was analyzed using an automated Bernard calcimeter, and the grain size analyses were performed with a Malvern Supersizer "S" at the Université Bordeaux 1. Detailed data are reported in St-Onge et al. (2004).

the magnetic particles being plastered horizontally because of high flow velocity and rapid and thick sediment accumulation. These layers are interpreted either as mono-event deposits (turbidite) or bi-event deposits (turbidite+hyperpycnite). In light of the geological, sedimentological and hydrological setting of the Saguenay Fjord, St-Onge et al. (2004) concluded that these RDLs were likely all triggered, either directly or indirectly, by strong earthquakes. The mono-event RDLs resulted from earthquake-triggered slides that became turbidity currents, whereas the bi-event RDLs resulted from similar events combined with the breaching and rapid draining, during the spring freshet, of a natural dam generated by an earthquake-triggered landslide.

4.3. CAT-Scan Analysis as a Millimeter-Scale Paleoceanographic Tool

In this section, we further illustrate how CAT-scan analysis can be applied to sedimentary sequences to produce a continuous mm-scale paleoclimatic tool that can be used to identify millennial- to seasonal-scale climatic oscillations, using examples from two IMAGES Calypso piston cores from the St. Lawrence Estuary (Eastern Canada). CAT-scan analysis of the two Calypso cores was performed on 1.5 m core sections using a medical GE 7590 K Hi-speed Advantage 2.X CT/i CAT-scanner at the *Centre Hospitalier Régional de Rimouski*, Québec, Canada, in 1999. Longitudinal images were obtained using a source radiation of 120 keV and 45 mA. These images show average linear attenuation coefficients integrated over the total thickness of the scanned object (the core diameter: ~11.5 cm) and shown a plane view. The dimensions of each longitudinal image are 512 × 296 pixels, which corresponds to a pixel size of 1.015 mm. For each core section, five images of 300-mm long segments were thus acquired. Continuous images of both Calypso cores were then constructed using the Igor™ software by creating a matrix for each image and incorporating each image matrix into the final matrix of each core. Using the same software, a continuous profile of the mean pixel intensity (CT number) over a width of ~2 cm was then extracted from the newly constructed image. An artefact associated with the

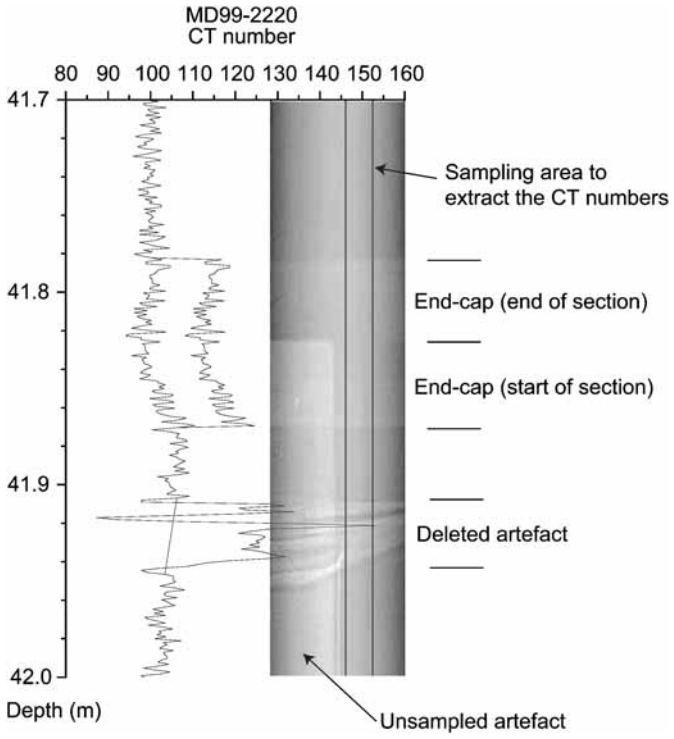

Figure 19 Examples of artefacts resulting from the presence of the examination table and the end-caps, and uncorrected (right curve) and corrected (left curve) extracted CT numbers for core 2220.

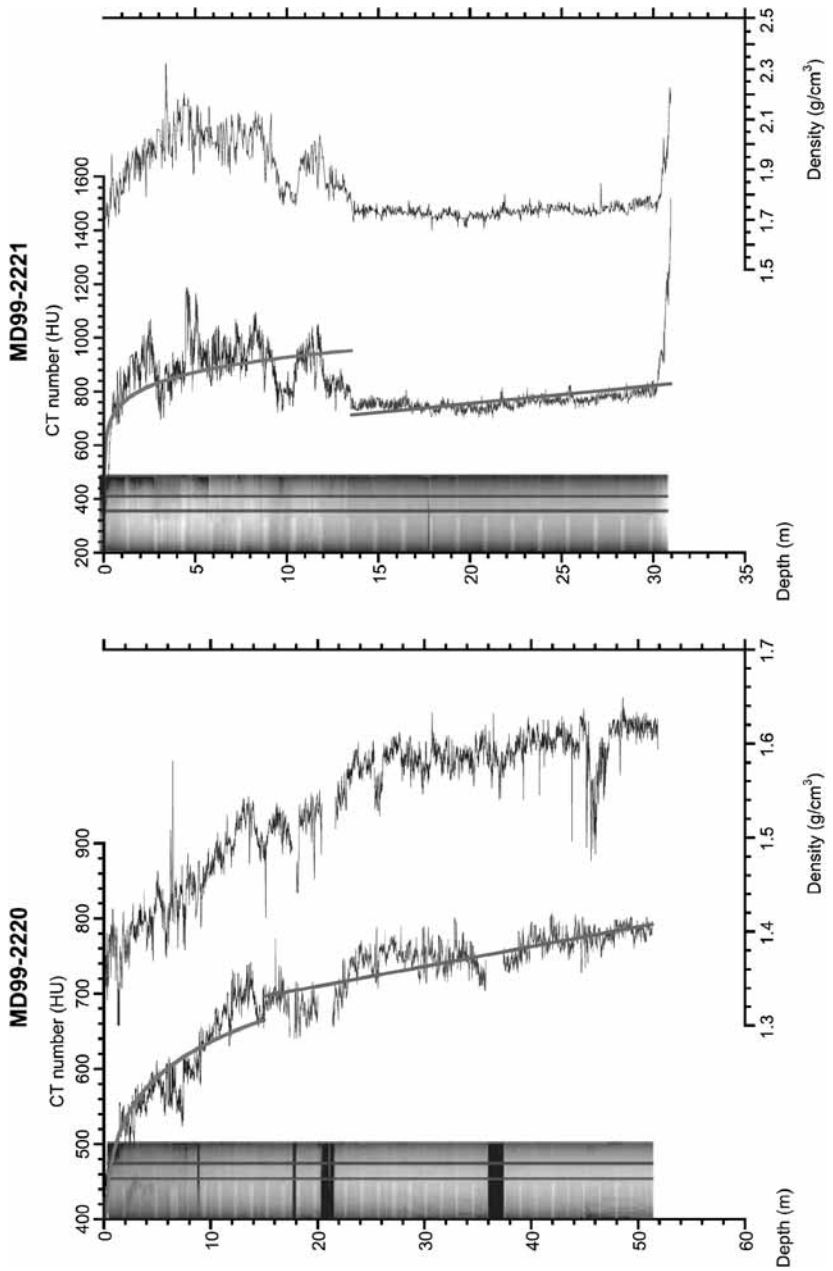

Figure 20 Longitudinal CAT-scan images and corrected extracted CT number profiles for cores 2220 (A) and 2221 (B) compared with bulk density measurements obtained onboard the *Marion Dufresne II* with a GEOTEK MSCL at 2-cm intervals. A logarithmic trend (upper part of the curve in postglacial sediments) and a linear trend (lower part of the curve in glaciomarine sediments), probably associated with sediment consolidation, are also visible. A sandy layer at the base of core 2221 was excluded from the linear fit. The areas delineated by two vertical lines on both core images are the sampling areas over which CT numbers were extracted.

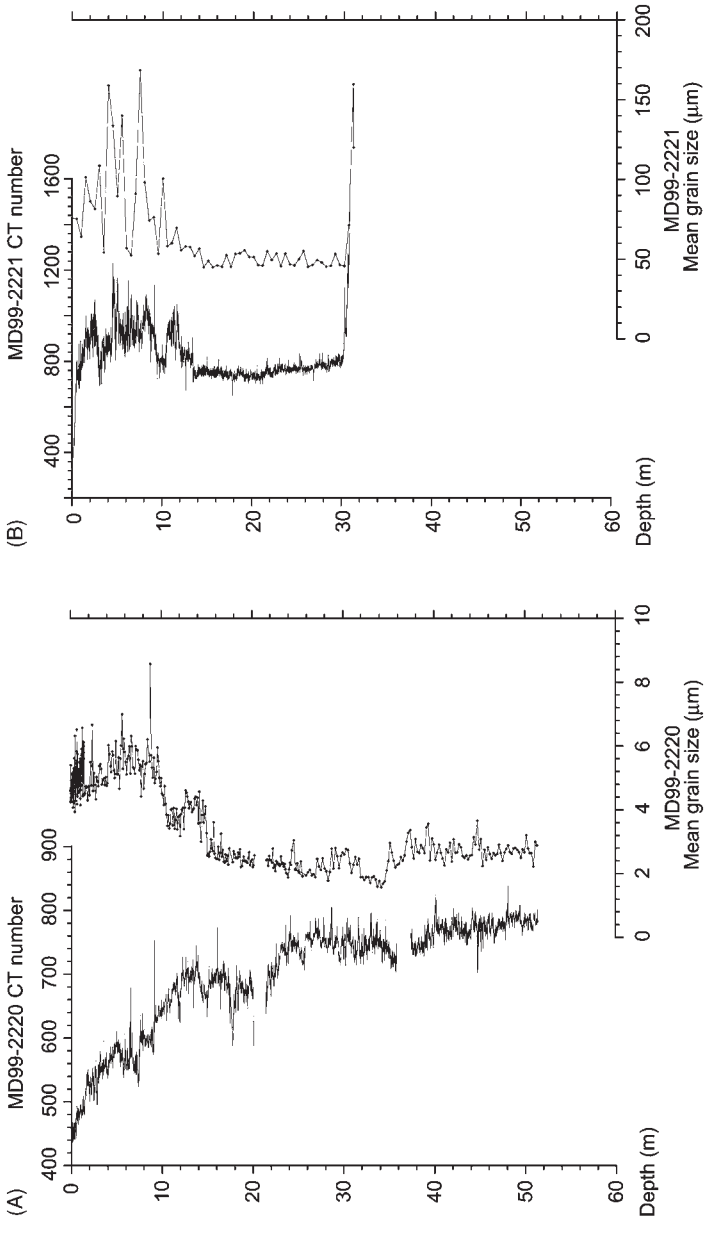

Figure 21 Comparison of CT profiles and grain size for cores MD99-2220 (A) and MD99-2221 (B). Grain size measurements were made using a Coulter Counter™ TAII analyzer at the Geological Survey of Canada (Atlantic), for core MD99-2220, and a Fritsch™ Analysette 22 laser diffraction analyzer at the INRS-ETE in Québec City, for core MD99-2221.

examination table is apparent on the first image of each core section and was only partially sampled by our procedure (Figure 19). In addition, erroneous CT numbers associated with this artefact were deleted from the continuous profile (Figure 19). Because the images were obtained in a clean hospital setting, the end-caps of the different sections could not be removed and resulted in another artefact, which slightly increased CT numbers. We corrected each core section for this small offset by visually adjusting the CT number profiles (Figure 19). Because of the CAT-scan medical software limitations, CT numbers obtained on the longitudinal images are not Hounsfield units (HU). A first-order empirical relationship between the CT numbers of the longitudinal and transverse images (in HU) at the same depth was therefore determined (Cagnat, 2004) for both Calypso cores and is as follows:

$$CT_L = 195 \ln CT_T - 1194, \quad r^2 = 0.85 \tag{2}$$

where CT_L is the CT number extracted from the longitudinal image and CT_T, the CT number, in HU, extracted from the transverse image.

In the CT number profiles of cores MD99-2220 and MD99-2221 shown in Figure 20, postglacial and glaciomarine sediments are readily distinguished (St-Onge, Stoner, & Hillaire-Marcel, 2003). Figure 20 also highlights the coarser-grained nature of postglacial sediments in core MD99-2221 (average CT number of 882 ± 109) compared to core MD99-2220 postglacial sediments (average CT number of 599 ± 70; see also Figure 21). Postglacial sediments in both cores are characterized by cyclic and high frequency oscillations superimposed on a long-term logarithmic trend, whereas glaciomarine sediments are characterized by high frequency variations superimposed on a long-term linear trend. Because these long-term trends are not seen in the grain size profiles (Figure 21), we interpret them to reflect the effect of sediment consolidation, which reduces porosity and thus increases CT number. These long-term trends are also seen in bulk density profiles (see below). In Figure 20, the CT number profiles of cores 2220 and 2221 are also compared to bulk density profiles measured onboard the RV *Marion Dufresne II* using a GEOTEK MSCL at 2 cm intervals. The overall agreement between density and CT number profiles suggests that the latter reflect variations in bulk density and could therefore be used as a mm-scale proxy (1.015-mm resolution) for sedimentological changes. Indeed, after removal of the long-term trends associated with sediment consolidation, spectral analysis of the CAT-scan data for the postglacial sediments revealed millennial- to centennial-scale oscillations, whereas spectral analysis of the glaciomarine sequences revealed decadal to annual cycles (St-Onge and Long, in review). Moreover, CAT-scan analysis of a Sangamonian sequence drilled onshore in the St. Lawrence Middle Estuary revealed similar decadal to annual cycles, as well as seasonal cycles possibly associated to tidal amplitude variations (Boespflug et al., 1995).

5. Conclusion

Continuous measurements of the physical properties of sediments now form the basis of most paleoceanographic campaign, providing quantitative information on long

sediment cores at resolutions generally on the cm-scale. Most methods routinely used onboard research vessels such as the typical sensors mounted on a MSCL allow fast and nondestructive analysis and may, for instance, be used directly for core logging and stratigraphic description. The last decade has seen the development and use of methods such as high-resolution digital core imaging, micro X-ray fluorescence, CAT-scan, digital X-ray imaging, MRI and confocal macroscopy and microscopy which can achieve millimeter- to micrometer-scale downcore resolutions. These high resolutions are now used to study seasonal- to millennial-scale processes. Further technological development of methods such as CAT-scan, digital imaging and X-ray imaging will likely lead to further increase in resolution. For instance, the latest generation of medical CAT-scan instruments already produce pixel resolutions an order of magnitude higher than those of CAT-scan images presented in this paper. Several manufacturers and research groups are also working toward making some of these techniques directly available for shipboard measurements. Finally, efforts should also go toward integrating the vast amounts of data collected with this new generation of sensors into specially designed databases in order to facilitate the comparison and extraction of data, thus allowing paleoceanographers to focus on interpretation. However, these new developments are not necessarily designed by and for geoscientists, and collaboration will thus be necessary to ensure their useful transfer to the geoscience community.

ACKNOWLEDGMENTS

G. St-Onge dedicates this chapter to the memory of Gaston Desrosiers (ISMER), a friend and colleague, as well as a pioneer in the use of CAT-scan analysis in benthic ecology. We are in debt to Peter Schultheiss (GEOTEK), Frank Rack (Joint Oceanographic Institutions), Bruce Balcom (University of New Brunswick), Ian Snowball (Lund University), Jacques Labrie (INRS-ETE), Robert Wheatcroft (Oregon State University), Robert Kleinberg (Schlumberger), Kinuyo Kanamaru (University of Massachusetts), Sébastien Zaragosi (Université Bordeaux 1), and Gaston Desrosiers and Suzanne Dufour (ISMER) for generously sharing preprints, reprints or some of the figures used in this chapter. Special thanks also go to Peter Schultheiss (GEOTEK) for providing technical information about the MSCL. We also thank Jacques Locat (Université Laval) for the cores presented in Figures 16 and 17 and for the "Saguenay post-déluge" project, as well as David J.W. Piper (Geological Survey of Canada-Atlantic) for a very detailed and constructive review. We wish to sincerely thank the IPEV, Yvon Balut, the captain, officers, crew and scientific participants of several IMAGES cruises on board the *R/V Marion Dufresne II*. This study was supported by NSERC Discovery grants to G. St-Onge and P. Francus. This constitutes UMR CNRS 5805 EPOC contribution 1582. The authors also acknowledge the acquisition of the ITRAX and CAT-scan presented in this paper through major grants from the Canadian Foundation for Innovation (CFI) to P. Francus and B. Long (INRS-ETE), respectively. This is GEOTOP-UQAM-McGill contribution.

REFERENCES

Adgebie, A. T., Schneider, R. R., Röhl, U., & Wefer, G. (2003). Glacial millennial-scale fluctuations in central African precipitation recorded in terrigenous sediment supply and freshwater signals offshore Cameroon. *Palaeogeography, Palaeoclimatology, Palaeoecology*, *197*, 323–333.

Amos, C. L., Sutherland, T. F., Radzijewski, B., & Doucette, M. (1996). A rapid technique to determine bulk density of fine-grained sediments by X-ray computed tomography. *Journal of Sedimentary Research*, *66*, 1023–1039.

Andres, M. S., Bernasconi, S. M., McKenzie, J. A., & Röhl, U. (2003). Southern Ocean deglacial record supports global Younger Dryas. *Earth and Planetary Science Letters*, *216*, 515–525.

Andrews, J. T., & Freeman, W. (1996). The measurement of sediment color using the colortron spectrophotometer. *Arctic and Alpine Research*, *28*, 524–528.

Arz, H. W., Gerhardt, S., Pätzold, J., & Röhl, U. (2001). Millennial-scale changes of surface- and deep-water flow in the western tropical Atlantic linked to Northern Hemisphere high-latitude climate during the Holocene. *Geology*, *29*, 239–242.

Arz, H. W., Pätzold, J., Müller, P. J., & Moammar, M. O. (2003). Influence of Northern Hemisphere climate and global sea level rise on the restricted Red Sea marine environment during termination I. *Paleoceanography*, *18*, 1053, doi:10.1029/2002PA000864.

Attard, J. J., McDonald, P. J., Roberts, S. P., & Taylor, T. (1994). Solid state NMR imaging of irreducible water in reservoir cores for spatially resolved pore surface relaxation estimation. *Magnetic Resonance Imaging*, *12*, 355–359.

Bahr, A., Lamy, F., Arz, H., Kuhlmann, H., & Wefer, G. (2005). Late glacial to Holocene climate and sedimentation history in the NW Black Sea. *Marine Geology*, *214*, 309–322.

Balsam, W. L., Damuth, J. E., & Schneider, R. R. (1997). Comparison of shipboard vs. shore-based spectral data from Amazon fan cores: implications for interpreting sediment composition. In: R. D. Flood, D. J. W. Piper, A. Klaus & L. C. Peterson (Eds), *Proceedings of Ocean Drilling Program, Scientific Reports 155* (pp. 1–23). Texas: College Station (Ocean Drilling Program).

Balsam, W. L., & Deaton, B. C. (1991). Sediment dispersal in the Atlantic Ocean: Evaluation by visible light spectra. *Reviews in Aquatic Sciences*, *4*, 411–447.

Baumann, T., Petsch, R., Fesl, G., & Niessner, R. (2002). Flow and diffusion measurements in natural porous media using magnetic resonance imaging. *Journal of Environmental Quality*, *31*, 470–476.

Berns, R. S. (2000). *Billmeyer and Saltzman's principles of color technology* (p. 247). New York: Wiley.

Blum, P. (1997). *Physical properties handbook: A guide to the shipboard measurement of physical properties of deep-sea cores* (Ocean Drilling Program Technical Note 26). Retrieved from http://www-odp.tamu.edu/publications/tnotes/tn26/TOC.HTM.

Blum, P., Rabaute, A., Gaudon, P., & Allan, J. F. (1997). Analysis of natural gamma-ray spectra obtained from sediment cores with the shipboard scintillation detector of the Ocean Drilling Program: Example from Leg 156. *Proceedings of the Ocean Drilling Program, Scientific Results*, *156*, 183–195.

Boespflug, X., Long, B. F. N., & Occhietti, S. (1995). CAT-scan in marine stratigraphy: A quantitative approach. *Marine Geology*, *122*, 281–301.

Bouma, A. H. (1962). *Sedimentology of some flysch deposits. A graphic approach to facies interpretation* (p. 168). Amsterdam: Elsevier.

Bouma, A. H. (1969). *Methods for the Study of Sedimentary Structures* (p. 458). Wiley: New York

Boyle, E. A. (1997). Characteristics of the deep ocean carbon system during the past 150,000 years: ΣCO_2 distributions, deep water flow patterns and abrupt climate change. *Proceedings of National Academy of Sciences, U.S.A.*, *94*, 8300–8307.

Bozzano, G., Kuhlmann, H., & Alonso, B. (2002). Storminess control over African dust input to the Moroccan Atlantic margin (NW Africa) at the time of maxima boreal summer insolation: A record of the last 220 kyr. *Palaeogeography, Palaeoclimatology, Palaeoecology*, *183*, 155–168.

Cagnat, E. (2004). Étude sédimentologique de la série holocène de l'estuaire maritime du Saint-Laurent: apport de la tomodensitométrie. M.Sc. Mémoire, INRS-ETE, Québec, Canada.

Champanhet, J. M., Durand, J., Long, B., & Laberye, B. (1989). Apport du scanner à la définition géométrique des réservoirs non consolidés. *Bulletin des centres de recherche exploration-production Elf-Aquitaine*, *13*, 167–174.

Chapman, M. R., & Shackleton, N. J. (2000). Evidence of 550-year and 1000-year cyclicities in North Atlantic circulation patterns during the Holocene. *The Holocene*, *10*, 287–291.

Chen, Q., Rack, F., & Balcom, B. (2006). Quantitative magnetic resonance imaging methods for core analysis. In: R. G. Rothwell (Ed.), *New ways of looking at sediment cores and core data* (pp. 193–207). London: Geological Society (Special Publication).

Cheshire, H., Thurow, J., & Nederbragt, A. J. (2005). Late Quaternary climate change record from two long sediment cores from Guaymas Basin, Gulf of California. *Journal of Quaternary Science*, *20*, 457–469.

Chmelick, F. B. (1967). Electro-osmotic core cutting. *Marine Geology, 5*, 321–325.
Crémer, J.-F., Long, B., Desrosiers, G., de Montety, L., & Locat, J. (2002). Application de la scanographie à l'étude de la densité des sédiments et à la caractérisation des structures sédimentaires: Exemple des sédiments déposés dans la rivière Saguenay (Québec, Canada) après la crue de juillet de 1996. *Canadian Geotechnical Journal*, *39*, 440–450.
Croudace, I. W., Rindby, A., & Rothwell, R. G. (2006). ITRAX: Description and evaluation of a new X-ray core scanner. In: R. G. Rothwell (Ed.), *New ways of looking at sediment cores and core data* (pp. 51–63). London: Geological Society (Special Publication).
Davies, S., Hardwick, A., Roberts, D., Spowage, K., & Packer, K. J. (1994). Quantification of oil and water in preserved reservoir rock by NMR spectroscopy and imaging. *Magnetic Resonance Imaging*, *12*, 349–353.
Deaton, B. C., & Baslam, W. L. (1991). Visible spectroscopy: A rapid method for determining hematite and goethite concentrations in geological material. *Journal of Sedimentary Petrology, 61*, 628–632.
Debret, M., Desmet, M., Balsam, W., Copard, Y., Francus, P., & Laj, C. (2006). Spectrophotometer analysis of Holocene sediments from an anoxic fjord: Saanich Inlet, Bristish Columbia, Canada. *Marine Geology, 229*, 15–28.
Dixon, A. E., & Damaskinos, S. (1998). *Apparatus and method for scanning laser imaging of macroscopic samples*. US Patent 5,760,951.
Dixon, A. E., Damaskinos, S., Ribes, A., & Beesley, K. M. (1995). A new confocal scanning beam laser macroscope using a telecentric f-theta laser scan lens. *Journal of Microscopy, 178*, 261–266.
Dufour, S. C., Desrosiers, G., Long, B., Lajeunesse, P., Gagnoud, M., Labrie, J., Archambault, P., & Stora, G. (2005). A new method for three-dimensional visualization and quantification of biogenic structures in aquatic sediments using axial tomodensitometry. *Limnology and Oceanography: Methods*, *3*, 372–380.
Duliu, O. (1999). Computer axial tomography in geosciences: An overview. *Earth Science Reviews*, *48*, 265–281.
Evans, M.E., Heller, F. (2003). *Environmental Magnetism: Principles and Applications of Enviromagnetics* (p. 299). San Diego: Academic Press.
Francus, P. (Ed.) (2004). *Image Analysis, Sediments and Paleoenvironments* (p. 330). Dordrecht: Kluwer Academic Publishers.
Funk, J. A., von Dobeneck, T., & von Reitz, A. (2004a). Integrated rock magnetic and geochemical quantification of redoxmorphic iron mineral diagenesis in Late Quaternary sediments from the equatorial Atlantic. In: G. Wefer, S. Mulitza & V. Ratmeyer (Eds), *The South Atlantic in the Late Quaternary* (pp. 237–260). Dordrecht: Springer.
Funk, J. A., von Dobeneck, T., von Wagner, T., & Kasten, S. (2004b). Late Quaternary sedimentation and early diagenesis in the equatorial Atlantic Ocean: Pattern, trends, and processes deduced from rock magnetic and geochemical records. In: G. Wefer, S. Mulitza & V. Ratmeyer (Eds), *The South Atlantic in the Late Quaternary* (pp. 461–497). Dordrecht: Springer.
Gingras, M. K., MacMillan, B., Balcom, B., Saunders, T., & Pemberton, G. (2002). Using magnetic resonance imaging and petrographic techniques to understand the textural attributes and porosity distribution in *Macronichnus*-burrowed sandstone. *Journal of Sedimentary Research*, *72*, 552–558.
Grützner, J., Hillenbrand, C.-D., & Rebesco, M. A. (2005). Terrigenous flux and biogenic silica deposition at the Antarctic continental rise during the late Miocene to early Pliocene: Implications for ice sheet stability and sea ice coverage. *Global and Planetary Change*, *45*, 131–149.
Harris, S. E., Mix, A. C., & King, T. (1997). Biogenic and terrigenous sedimentation at Ceara Rise, western tropical Atlantic, supports Pliocene-Pleistocene deep-water linkage between hemispheres. In: N. J. Shackleton, W. B. Curry, C. Richter & T. J. Bralower (Eds), *Proceedings of Ocean Drilling Program, Scientific Reports 154* (pp. 331–348). Texas: College Station (Ocean Drilling Program).
Helmke, J. P., Bauch, H. A., Röhl, U., & Mazaud, A. (2005). Changes in sedimentation patterns of the Nordic seas region across the mid-Pleistocene. *Marine Geology, 215*, 107–122.
Helmke, J. P., Schulz, M., & Bauch, H. A. (2002). Sediment-color record from the Northeast Atlantic reveals patterns of millennial-scale climate variability during the Past 500,000 years. *Quaternary Research*, *57*, 49–57.

Hepp, D. A., Mörz, T., & Grützner, J. (2006). Pliocene glacial cyclicity in deep-sea sediment drifts (Antarctic Peninsula Pacific Margin). *Palaeogeography, Palaeoclimatology, Palaeoecology.*, *231*, 181–198.

Holler, P., & Kögler, F. C. (1990). Computer tomography: A non destructive, high resolution technique for investigation of sedimentary structures. *Marine Geology*, *91*, 263–266.

Holyer, R. J., Young, D. K., Sandidge, J. C., & Briggs, K. B. (1996). Sediment density structure derived from textural analysis of cross-sectional X-radiographs. *Geo-Marine Letters*, *16*, 204–211.

Jaccard, S. L., Haug, G. H., Sigman, D. M., Pedersen, T. F., Thierstein, H. R., & Röhl, U. (2005). Glacial/interglacial changes in Subarctic North Pacific stratification. *Science*, *308*, 1003–1006.

Jackson, P. D., Briggs, K. B., & Flint, R. C. (1996). Evaluation of sediment heterogeneity using microresistivity imaging and X-radiography. *Geo-Marine Letters*, *16*, 219–225.

Kantzas, A., Marentette, D., & Jha, K. N. (1992). Computer-assisted tomography: From qualitative visualization to quantitative core analysis. *Journal of Petroleum Technology*, *31*, 48–56.

Keigwin, L. D., & Pickart, R. S. (1999). Slope water current over the Laurentian fan on interannual to millennial time scales. *Science*, *286*, 520–523.

Ketcham, R., & Carlson, W. A. (2001). Acquisition, optimization and interpretation of X-ray computed tomographic imagery: Applications to the geosciences. *Computers & Geosciences*, *27*, 381–400.

Kleinberg, R. L., & Griffin, D. D. (2005). NMR measurements of permafrost: Unfrozen water assay, pore scale distribution of ice, and hydraulic permeability of sediments. *Cold Regions Science and Technology*, *42*, 63–77.

Kuhlmann, H., Freudenthal, T., Helmke, P., & Meggers, H. (2004a). Reconstruction of paleoceanography off NW Africa for the last 40,000 years: Influence of local and regional factors on sediment accumulation. *Marine Geology*, *207*, 209–234.

Kuhlmann, H., Meggers, H., Freudenthal, T., & Wefer, G. (2004b). The transition of the monsoonal and the North Atlantic climate system off NW Africa during the Holocene. *Geophysical Research Letters*, 31, L22204, doi:10.1029/2004GL021267.

Lamy, F., Hebbeln, D., Röhl, U., & Wefer, G. (2001). Holocene rainfall variability in southern Chile: A marine record of latitudinal shifts of the Southern Westerlies. *Earth and Planetary Science Letters*, *185*, 369–382.

Lapointe, M. F., Secretan, Y., Driscoll, S. N., Bergeron, N., & Leclerc, M. (1998). Response of the Ha!Ha! River to the flood of July 1996 in the Saguenay Region of Quebec: Large-scale avulsion in a glaciated valley. *Water Resources Research*, *34*, 2383–2392.

Lofi, J., & Weber, O. (2001). SCOPIX–digital processing of X-ray images for the enhancement of sedimentary structures in undisturbed core slabs. *Geo-Marine Letters*, *20*, 182–186.

Maher, B. A., Thompson, R. (1999). *Quaternary climates, environments and magnetism* (p. 390). Cambridge: Cambridge University Press.

Mansfield, P., & Issa, B. (1996). Fluid transport in porous rocks. I. EPI studies and a stochastic model of flow. *Journal of Magnetic Resonance A*, *122*, 137–148.

Marica, F., Chen, Q., Hamilton, A., Hall, C., Al, T., & Balcom, B. J. (2006). Spatially resolved measurement of rock core porosity. *Journal of Magnetic Resonance*, *178*, 136–141.

Mees, F., Swennen, R., Van Geet, M., & Jacobs, P. (2003). *Applications of X-ray computed tomography in the geosciences* (p. 243). London: Geological Society (Special Publications 215).

Mermillod-Blondin, F., Marie, S., Desrosiers, G., Long, B., de Montety, L., Michaud, E., & Stora, G. (2003). Assessment of the spatial variability of intertidal benthic communities by axial tomodensitometry: Importance of fine-scale heterogeneity. *Journal of Experimental Marine Biology and Ecology*, *287*, 193–208.

Michaud, E., Desrosiers, G., Long, B., de Montety, L., Crémer, J. -F., Pelletier, E., Locat, J., Gilbert, F., & Stora, G. (2003). Use of axial tomography to follow temporal changes of benthic communities in an unstable sedimentary environment (Baie des Ha!Ha!, Saguenay Fjord). *Journal of Experimental Marine Biology and Ecology*, 285/286, 265–282.

Migeon, S. (2000). *Dunes géantes et levées sédimentaires en domaine marin profond: approche morphologique, sismique et sédimentologique*. Ph.D. Thesis, Université Bordeaux 1, p. 288.

Migeon, S., Savoye, B., Zanella, E., Mulder, T., Faugères, J.-C., & Weber, O. (2001). Detailed seismic and sedimentary study of turbidite sediment waves one the Var sedimentary ridge (SE France):

Significance for sediment transport and deposition and for the mechanism of sediment wave construction. *Marine and Petroleum Geology, 18*, 179–208.

Migeon, S., Weber, O., Faugères, J.-C., & Saint-Paul, J. (1999). SCOPIX: A new X-ray imaging system for core analysis. *Geo-Marine Letters*, *18*, 251–255.

Mix, A. C., Harris, S. E., & Janecek, T. R. (1995). Estimating lithology from non intrusive reflectance spectra: Leg 138. In: N. G. Pisias, L. A. Mayer, T. R. Janecek, A. Palmer-Julson & T. H. van Andel (Eds), *Proceedings of Ocean Drilling Program, Scientific Reports 138* (pp. 413–427). Texas: College Station (Ocean Drilling Program).

Mix, A. C., Rugh, W., Pisias, N. G., Veirs, S., Leg 138 Shipboard Sedimentologists, & Leg 138 Scientific Party (1992). Color Reflectance spectroscopy: A tool for rapid characterisation of deep-sea sediments. In: N. G. Pisias, L. A. Mayer, T. R. Janecek, A. Palmer-Julson & T. H. van Andel (Eds), *Proceedings of ocean drilling program, initial reports 138* (pp. 67–77). Texas: College Station (Ocean Drilling Program).

Moy, C. M., Seltzer, G. O., Rodbell, D. T., & Anderson, D. M. (2002). Variability of El Nino/Southern Oscillation activity at millennial timescales during the Holocene epoch. *Nature*, *420*, 162–165.

Mulder, T., Migeon, S., Savoye, B., Faugères, J.-C. (2001a). Inversely graded turbidite sequences in the deep Mediterranean: A record of deposits from flood-generated turbidity currents? *Geo-Marine Letters, 21*, 86–93

Mulder, T., Migeon, S., Savoye, B., & Faugères, J.-C. (2002). Inversely graded turbidite sequences in the deep Mediterranean: A record of deposits from flood-generated turbidity currents? Reply. *Geo-Marine Letters*, *22*, 112–120.

Mulder, T., Migeon, S., Savoye, B., & Jouanneau, J.-M. (2001b). Twentieth century floods recorded in deep Mediterranean sediments. *Geology, 29*, 1011–1014.

Mulder, T., & Syvitski, J. P. M. (1995). Turbidity currents generated at river mouths during exceptional discharges to the world oceans. *Journal of Geology, 103*, 285–299.

Mulder, T., Syvitski, J. P. M., Migeon, S., Faugères, J.-C., & Savoye, B. (2003). Marine hyperpycnal flows: Initiation, behavior and related deposits. A review. *Marine and Petroleum Geology, 20*, 861–882.

Mulder, T., Syvitski, J. P. M., & Skene, K. I. (1998). Modelling of erosion and deposition by turbidity currents generated at river mouths. *Journal of Sedimentary Research*, *68*, 124–137.

Mulder, T., Weber, O., Anschutz, P., Jorissen, F. J., & Jouanneau, J.-M. (2001c). A few months-old storm-generated turbidite deposited in the Capbreton Canyon (Bay of Biscay, S-W France). *Geomarine Letters*, *21*, 149–156.

Nederbragt, A. J., & Thurow, J. W. (2004). Digital sediment colour analysis as a method to obtain high resolution climate proxy records. In: P. Francus (Ed.), *Image analysis, sediments, and paleoenvironments* (p. 330). Dordrecht: Kluwer Academic Publishers.

Orsi, T. H., Edwards, C. M., & Anderson, A. L. (1994). X-ray computed tomography: A non-destructive method for quantitative analysis of sediment cores. *Journal of Sedimentary Research A*, *64*, 690–693.

Ortiz, J. D., Mix, A., Harris, S., & O'Connell, S. (1999). Diffuse spectral reflectance as a proxy for percent carbonate content in North Atlantic sediments. *Paleoceanography, 14*, 171–186.

Ortiz, J. D., & Rack, F. R. (1999). Non-invasive sediment monitoring methods: Current and future tools for high-resolution climate studies. In: F. Abrantes & A. C. Mix (Eds), *Reconstructing ocean history: A window into the future* (pp. 343–380). New York: Kluwer/Plenum.

Peterson, L. C., Haug, G. H., Hughen, K. A., & Röhl, U. (2000). Rapid changes in the hydrologic cycle of the tropical Atlantic during the last glacial. *Science*, *290*, 1947–1951.

Principato, S. M. (2004). X-radiographs of sediment cores: A guide to analyzing diamicton. In: P. Francus (Ed.), *Image Analysis, Sediments and Paleoenvironments* (pp. 165–185). Dordrecht: Kluwer Academic Publishers.

Rack, F. R. (1998). *Tomorrow's technology today.* Interim report of the IMAGES standing committee on "New technologies in sediment imaging", p. 33.

Rack, F. R., Balcom, B. J., MacGregor, R. P., & Armstrong, R. L. (1997). Magnetic resonance imaging of the Lake Agassiz–Lake Winnipeg transition. *Journal of Paleolimnology, 19*, 255–264.

Rack, F. R., Ribes, A. C., Tsintzouras, G., Marshall, G., Damaskinos, S., & Dixon, A. E. (1998). Preliminary results from biomedical imaging of lake and ocean sediments. *Proceedings of the Sixth International Conference on Paleoceanography*, August 24–28, Lisbon, Portugal, p. 189.

Ribes, A. C., Damaskinos, S., & Dixon, A. E. (1995). Photoluminescence imaging of porous silicon using a confocal scanning laser macroscope/microscope. *Applied Physics Letters*, *66*, 2321–2323.

Ribes, A. C., Damaskinos, S., Tiedje, H. F., Dixon, A. E., & Brodie, D. E. (1996). Reflected light, photoluminescence, and OBIC imaging of solar cells using a confocal scanning laser macroscope/microscope. *Solar Energy Materials and Solar Cells*, *44*, 439–450.

Ribes, A. C., Lundberg, J., Waldron, D. J., Vesely, M., Damaskinos, S., Guthrie, S. I., & Dixon, A. E. (2000). Photoluminescence imaging of speleothem microbanding with a high resolution confocal scanning laser macroscope. *Quaternary International*, *68–71*, 253–259.

Ribes, A. C., Marshall, G., Tsintzouras, G., Damaskinos, S., Dixon, A. E., & Rack, F. R. (1998). The confocal scanning beam MACROscope/Microscope applied to imaging ocean/lake core geological specimens. *Canadian Association of Physicists (CAP) annual meeting*, June 15, 1998, Waterloo, Canada, Physics in Canada 54, 10.

Röhl, U., Brinkhuis, H., & Fuller, M. (2004). On the search for the Paleocene/Eocene boundary in the Southern Ocean: Exploring ODP Leg 189 Holes 1171D and 1172D. In: N. F. Exon, M. Malone & J. P. Kennett (Eds), *The Cenozoic Southern Ocean and climate change between Australia and Antarctica* (pp. 113–126). American Geophysical Union, Geophysical Monograph Series 181.

Röhl, U., Brinkhuis, H., Fuller, M., Schellenberg, S. A., Stickley, C. E., & Williams, G. L. (2004). Cyclostratigraphy of middle and late Eocene sediments drilled on the East Tasman Plateau (Site 1172). In: N. F. Exon, M. Malone & J. P. Kennett (Eds), *Climate evolution in the Southern Ocean and Australia's Cenozoic flight northward from Antarctica* (pp. 127–152). American Geophysical Union, Geophysical Monograph Series 181.

Rothwell, R. G., Hoogakker, B., Thomson, J., & Croudace, I. W. (2006). Turbidite emplacement on the southern Balearic Abyssal Plain (Western Mediterranean Sea) during Marine Isotope Stages 1–3: An application of XRF scanning of sediment cores in lithostratigraphic analysis. In: R. G. Rothwell (Ed.), *New ways of looking at sediment cores and core data* (pp. 79–98). London: Geological Society (Special Publication).

Smith, J. N., & Schafer, C. (1987). A 20th-century record of climatologically modulated sediment accumulation rates in a Canadian fjord. *Quaternary Research*, *27*, 232–247.

Smith, J. N., & Walton, A. (1980). Sediment accumulation rates and geochronologies measured in the Saguenay Fjord using Pb-210 dating method. *Geochimica et Cosmochimica Acta*, *44*, 225–240.

Stevens, A. W., Wheatcroft, R. A., & Wiberg, P. L. (2007). Seabed properties and sediment erodibility along the western Adriatic margin, Italy. *Continental Shelf Research*, *27*, 400–416.

Stoner, J. S., Channell, J. E. T., & Hillaire-Marcel, C. (1996). The magnetic signature of rapidly deposited detrital layers from the deep Labrador Sea: Relationship to North Atlantic Heinrich layers. *Paleoceanography*, *11*, 309–325.

St-Onge, G., & Hillaire-Marcel, C. (2001). Isotopic constraints of sedimentary inputs and organic carbon burial rates in the Saguenay Fjord, Quebec. *Marine Geology*, *176*, 1–22.

St-Onge, G., & Long, B. (in review). CAT-scan analysis of sedimentary sequences: an ultrahigh-resolution paleoclimatic tool. *Engineering Geology*.

St-Onge, G., Mulder, T., Piper, D. J. W., Hillaire-Marcel, C., & Stoner, J. S. (2004). Earthquake and flood-induced turbidites in the Saguenay Fjord (Québec): A Holocene paleoseismicity record. *Quaternary Science Reviews*, *23*, 283–294.

St-Onge, G., Stoner, J. S., & Hillaire-Marcel, C. (2003). Holocene paleomagnetic records from the St. Lawrence Estuary: Centennial- to millennial-scale geomagnetic modulation of cosmogenic isotopes. *Earth and Planetary Science Letters*, *209*, 113–130.

Stuut, J.-B. W., Prins, M. A., & Jansen, J. H. F. (2002b). Fast reconnaissance of carbonate dissolution based on the size distribution of calcareous ooze on Walvis Ridge, SE Atlantic Ocean. *Marine Geology*, *190*, 581–589.

Stuut, J.-B. W., Prins, M. A., Schneider, R. R., Weltje, G. J., Jansen, J. H. F., & Postma, G. (2002a). A 300-kyr record of aridity and wind strength in southwestern Africa: Inferences from grain-size distributions of sediments on Walvis Ridge, SE Atlantic. *Marine Geology*, *180*, 221–233.

Syvitski, J. P. M., & Schafer, C. T. (1996). Evidence for earthquake-triggered basin collapse in Saguenay Fjord, Canada. *Sedimentary Geology, 104*, 127–153.

Thomas, R. G., Guyodo, Y., & Channell, J. E. T. (2003). U channel track for susceptibility measurements. *Geochemistry, Geophysics, Geosystems*, *4*, 1050, doi:10.1029/2002GC000454.

Thomson, J., Croudace, I. W., & Rothwell, R. G. (2006). A geochemical application of the ITRAX scanner to a sediment core containing eastern Mediterranean sapropel units. In: R. G. Rothwell (Ed.), *New ways of looking at sediment cores and core data* (pp. 65–77). London: Geological Society (Special Publication).

Thompson, R., & Oldfield, F. (1986). *Environmental magnetism*. Boston: Allen and Unwin p. 227.

Urgeles, R., Locat, J., Lee, H. J., & Martin, F. (2002). The Saguenay Fjord, Quebec, Canada: integrating marine geotechnical and geophysical data for seismic slope stability and hazard assessment. *Marine Geology, 185*, 319–340.

Vidal, L., Bickert, T., Wefer, G., & Röhl, U. (2002). Late Miocene stable isotope stratigraphy of SE Atlantic ODP Site 1085: Relation to Messinian events. *Marine Geology, 180*, 71–85.

Weber, M. E. (1998). Estimation of biogenic carbonate an opal by continuous non-destructive measurements in deep-sea sediments: Application to the eastern Equatorial Pacific. *Deep-Sea Research I, 45*, 1955–1975.

Wellington, S. L., & Vinegar, H. J. (1987). X-ray computerized tomography. *Journal of Petroleum Technology, 2*, 1951–1954.

West, S., Jansen, J. H. F., & Stuut, J.-B. (2004). Surface water conditions in the Northern Benguela Region (SE Atlantic) during the last 450 ky reconstructed from assemblages of planktonic foraminifera. *Marine Micropaleontology, 51*, 321–344.

Westerhold, T., Bickert, T., & Röhl, U. (2005). Middle to late Miocene oxygen isotope stratigraphy of ODP Site 1085 (SE Atlantic): New constraints on Miocene climate variability and sea-level fluctuations. *Palaeogeography, Palaeoclimatology, Palaeoecology, 217*, 205–222.

Wheatcroft, R. A., Stevens, A. W., Hunt, L. M., & Milligan, T. G. (2006). The large-scale distribution and internal geometry of the Fall 2000 Po River flood deposit: Evidence from digital X-radiography. *Continental Shelf Research*, *26*, 499–516.

Zaragosi, S., Bourillet, J.-F., Eynaud, F., Toucanne, S., Denhard, B., Van Toer, A., & Lanfumey, V. (2006). The impact of the last European deglaciation on the deep-sea turbidite systems of the Celtic-Armorican margin (Bay of Biscay). *Geo-Marine Letters*, *26*, 317–329.